This Book of Proceedings contains the extended abstracts of the contributions presented at the DIPSI Workshop 2022 on Droplet Impact Phenomena and Spray Investigation, organised by the University of Bergamo on Friday 1st July 2022 in Bergamo, Italy.

This workshop, which is now at its fourteenth edition, represents an important opportunity to share the recent knowledge on droplets and sprays in a variety of research fields and industrial applications.

The event is supported by the Department of Engineering and Applied Sciences of the University of Bergamo and the Research Training Group 2160/2 DROPIT in collaboration with the University of Stuttgart.

GIANPIETRO ELVIO COSSALI is full professor of thermal physics at the Department of Engineering and Applied Sciences of the University of Bergamo. His research activity is carried out in the field of thermo-fluid dynamics of multiphase systems, with particular reference to the characterization of sprays, to the dynamics of the interaction between droplets and solid and liquid surfaces and to the analytical modelling of heat and mass exchange in dispersed flows.

ISBN: 978-88-97253-09-9
DOI: 10.13122/DIPSI2022

CHALLENGE BASED LEARNING PER LO SPORT E IL TURISMO SOSTENIBILE

PROCEEDINGS
OF THE
DIPSI WORKSHOP 2022

Droplet Impact Phenomena & Spray Investigations

BERGAMO, ITALY, 1st JULY 2022

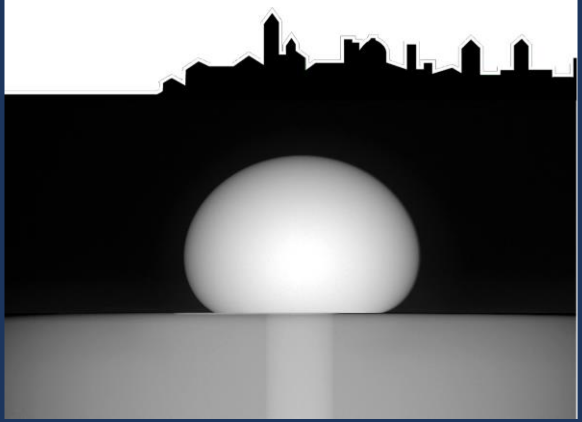

Edited by Gianpietro Elvio Cossali

UNIVERSITÀ
DEGLI STUDI
DI BERGAMO

2022

PROCEEDINGS
OF THE
DIPSI WORKSHOP 2022

Droplet Impact Phenomena
& Spray Investigations

BERGAMO, ITALY, 1st JULY 2022

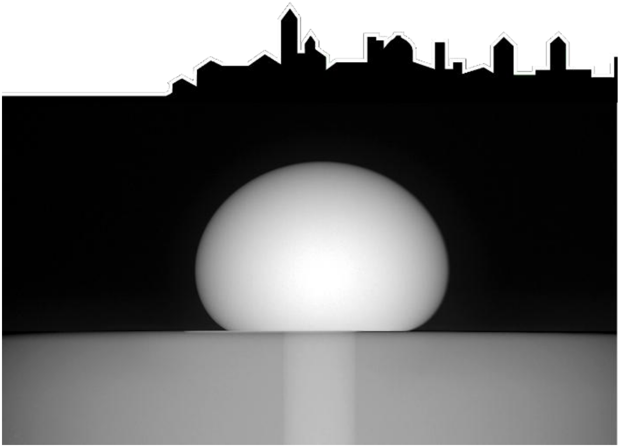

Edited by Gianpietro Elvio Cossali

Università degli Studi di Bergamo
2022

PROCEEDINGS OF THE DIPSI WORKSHOP 2022: Droplet Impact Phenomena & Spray investigations, Bergamo, Italy, 1st July 2022 / edited by Gianpietro Elvio Cossali – Bergamo: Università degli Studi di Bergamo, 2022.
ISBN: 978-88-97253-09-9
DOI: 10.13122/DPS 2022

Progetto grafico:
Servizi Editoriali – Università degli Studi di Bergamo
Università degli Studi di Bergamo
via Salvecchio, 19
24129 Bergamo
Cod. Fiscale 80004350163
P. IVA 01612800167

https://aisberg.unibg.it/handle/10446/234208

Workshop agenda, Friday 1st July 2022

08:45 Registration

09:00 Welcome speech

09:10 Invited lecture

9:10 C. Tropea, *The physics of aircraft icing.*

09:40 S1 Drop physics

09:40 S.S. Sazhin, D.V. Antonov, P.A. Strizhak, G. Castanet, E.A. Shchepakina, V.A. Sobolev and T. Bar-Kohany, *Puffing and micro-explosions in composite droplets: recent modelling results.*

10:05 D. Baumgartner, G. Brenn and C. Planchette, *Stretching separation in drop-drop and drop-jet collisions: theory and practical applications.*

10:30 Coffee break

11:00 S2 Measurement techniques

11:00 R. Clavenna, L. Araneo and A. Salerno, *Twin background subtraction: a simultaneous thermographic measure of thickness and temperature of a liquid film.*

11:25 R. Tadmor, *Solid-liquid work of adhesion.*

11:50 R. Akbari and C. Antonini, *Development of a robust open-source software for the automatic analysis of static and quasi-static contact angles.*

12:15 Lunch break

13:45 Poster session

R. Tietz, M.I. Pfeiffer and S. Fasoulas, *Symmetric simulations of droplets with a particle based Vlasov-Enskog-solver.*

Y. Stern, A. Vinod, V. Multanen and R. Tadmor, *Drops retracting while forming a rim.*

S. Schubert, *μ-PIV measurement of an impacting droplet onto a thin liquid film.*

D. Appel, J. Zeifang, A. Beck and C.-D. Munz, *Narrow band-based dynamic load balancing for multiphase flow simulations.*

A.K. Geppert, P. Foltyn and B. Weigand, *Effect of edge length and surface wettability on droplet impact onto a stand-alone cubic pillar.*

J. Stober and K. Schulte, *Numerical investigation of the mechanisms of early crown formation at an oblique drop impact onto a wall film.*

W. Ren, B. Weigand, M. Dumbser, *Numerical computation for drop impact on textured surfaces.*

P. Palmetshofer, P. Foltyn, A. Geppert and B. Weigand, *Dynamic contact angle measurements of droplets spreading on surfaces of varying wettability.*

M. Veyskarami, *Formation, growth and detachment of multiple droplets at the free flow-porous medium interface.*

S. Tonini, G.E. Cossali, E.A. Shchepakina, V.A. Sobolev, S.S. Sazhin, *A model of droplet evaporation: new mathematical developments.*

S. Tonini and G.E. Cossali, *Evaporation of multicomponent drops of general shape: analytical modelling through Stefan-Maxwell equations.*

14:30 S3 Sprays

14:30 M. Gajevic Joksimovic, I.V. Roisman, C. Tropea and J. Hussong, *Spray cooling of very hot substrates by multicomponent liquids.*

14:55 A. Amoresano, G. Langella and S. Roscioli, *On the mechanisms of sulfur capture by water spray systems.*

15:20 S4 Drop wall interaction

15:30 D.J. Bouchard, M. Andredaki, A. Georgoulas, S. Chandra and M. Marengo, *Droplet impact and flow into a gap between parallel plates: experimental and numerical analysis.*

15:45 H. Sontheimer, A. Gholijani, P. Stephan and T. Gambaryan-Roisman, *Coalescence of drops impacting a hot wall: hydrodynamics and heat transport*.

16:05 Coffee break

16:30 Workshop closure

Bergamo, 1st July 2022

Contents

Physics of Aircraft Icing

Cameron Tropea*
Institute of Fluid Mechanics and Aerodynamics, Technical University of Darmstadt, Germany
*Corresponding author: ctropea@sla.tu-darmstadt.de

Introduction

The certification of aircraft depends on demonstrating airworthiness under a variety of icing conditions related to both airframe icing and the icing in engines. Since in-flight experiments are not feasible due to safety reasons, the demonstration of airworthiness must rely on the use of validated predictive tools. It is therefore necessary to understand and describe the physical phenomena involved in ice accretion under the conditions prescribed by regulatory bodies, e.g. JAA, FAA, in order to formulate and implement reliable models into these tools. Whereas airframe icing occurs largely through the impact, freezing and accretion of liquid, possibly supercooled drops (SLD – supercooled large drops), icing in engines is more likely to occur due to ingestion of ice crystals encountered at higher altitudes (ICI – ice crystal icing). Whether drops or ice crystals, the specific phenomena of interest include the drop/ice crystal trajectory and probability or point of impact, the nucleation of drops to freeze or the shattering of ice crystals upon impact, the probability of residual mass remaining on the impact surface and the contribution to accretion, and the likelihood of accreted ice shedding from the surface. Ice accreted on the airframe or wing, will alter the aerodynamic performance and clearly represents a safety hazard. Ice crystal icing generally only occurs on heated surfaces such as warm compressor/turbine blades or heated instruments like a pitot tube. Here the shedding of accreted ice can lead to damage in the turbine or the accretion of ice can lead to false readings of the instrument, again both severe safety hazards. In the research directed toward aircraft icing, there is therefore a general distinction between icing due to liquid drops and icing due to ice crystals. More recently, attention has also been directed towards icing due to snowflakes, in particular related to the icing of intake grids on helicopter engine intakes. In the following description this distinction between SLD icing and ICI has also be adopted.

Icing arising from liquid drops

The reliability of predicting the trajectory of liquid drops placed in a velocity field is rather high and thus, the 'capture efficiency', i.e. the number of drops impacting a given surface, can be well predicted. This is done using an Euler-Lagrange approach, normally with a one-way coupling between the predicted velocity field around an aircraft or its components and the drops, assuming they are spheres. Typically, the relative velocities of drops in the airflow place the Reynolds number below the Newton regime for drag, i.e. Re<1000.

More challenging is the prediction of nucleation of a supercooled drop upon impact onto a cold surface. Nucleation is a highly stochastic phenomenon and can exhibit long delay times, even after the impact instant and even for drops well below the freezing temperature (Schremb et al., 2017). Once nucleated however, the freezing of a SLD takes on three stages. In the first stage, an ice layer rapidly forms along the underlying substrate, followed by the growth of dendrites throughout the bulk. In this stage of dendritic growth, the latent heat of solidification warms the supercooled bulk up to the melting temperature, typically involving 10-15% of the liquid volume for a supercooling of 8-15°C. Once the bulk is then at the melting temperature, the remaining liquid freezes according to a one-dimensional Stefan problem (Criscione et al., 2015). This freezing of an SLD is depicted graphically in Figure 1 (Schremb and Tropea, 2016).

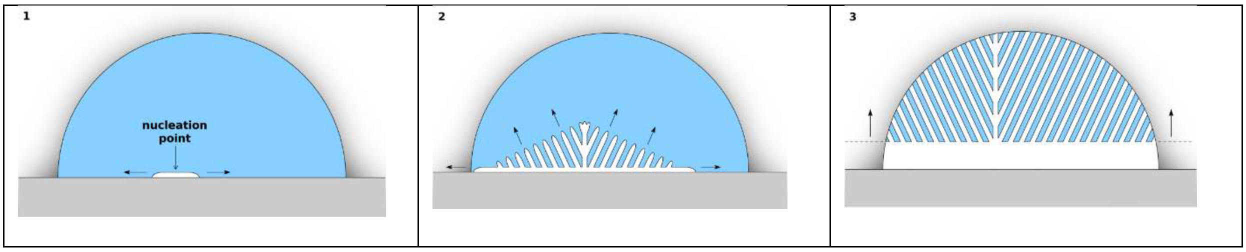

***Figure 1**: Schematic representation of the three stages of freezing of an SLD drop on a cold substrate, once nucleation has occurred.*

On the other hand, if a SLD impacts onto a frozen ice layer, then nucleation occurs immediately followed by the three stages of freezing. So the nucleation delay will determine to what extent the drop remains liquid after impact and, given the superimposed flow over the surface, for instance over the leading edge of a wing, the liquid may distribute over a wider area of the surface. This then determines how much ice accretes where, but remains a highly stochastic process, not easily amendable to prediction (Schremb et al., 2017).

Of particular interest is the deposited mass of the liquid drop, since a portion may splash and be re-emitted, to possibly impact further downstream. A portion may also flow away from the point of impact; thus, the hydrodynamics of drop impact play an important role in determining the drop spreading (Gloerfeld et al., 2021). In addition, the liquid properties, in particular the viscosity, may change significantly when in contact with the substrate and this will also influence the hydrodynamics. Despite these complexities, much progress has been made over recent years and the fundamental studies on single drop impact dynamics and thermodynamics have been augmented by large-scale tests in various icing wind tunnels.

Icing arising from ice crystals

While the prediction of trajectory and capture efficiency of ice particles is similar to that of liquid drops, two additional factors must be considered with ice crystal icing. For one, ICI occurs primarily on heated surfaces (Villedieu et al., 2019, Löwe et al., 2016). Second, the impact of a dry ice crystal onto a dry surface is different from that of a wetted ice crystal onto a dry surface or a wetted/dry ice crystal onto a wetted surface. The presence of liquid at the instance of impact can greatly influence the 'sticking efficiency', i.e. the probability that accretion will commence. For this reason, it is necessary to consider the possibility of an ice crystal beginning to melt before the instance of impact, for instance due to heating in an engine intake (Kintea et al., 2015). This involves evaluating the heat transfer to the ice crystal in the flow environment of the engine. Thus, the ratio of liquid water content (LWC) to total water content (TWC) will influence the icing severity, as pointed out by Currie et al. (2013). Too little water content will not be sufficient to lead to adhesion of the particle to the surface. Too much water content or too little ice will not cool the substrate sufficiently below the melting temperature to lead to an adhesion at the substrate ice interface. Approximate limits of LWC/TWC for ice accretion to occur are shown in Figure 2.

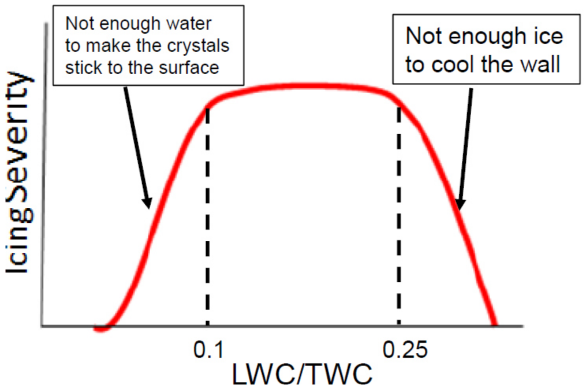

Figure 2: Icing severity as a function of LWC/TWC. Adapted from Currie et al. (2013).

Once an ice crystal impacts a substrate, it may shatter into smaller crystals and these then can again impact the heated surface, usually at much lower velocities and then the probability of partial melting and adhesion greatly increases. For this reason, an essential ingredient in modelling ICI is the fragmentation of ice crystals upon impact. Two typical video sequences of an ice crystal impact resulting in fragmentation is shown in **Figure 2**Figure 3 and modelling details can be found in Hauk et al. (2015), Reitter et al. (2022) and Roisman and Tropea (2015).

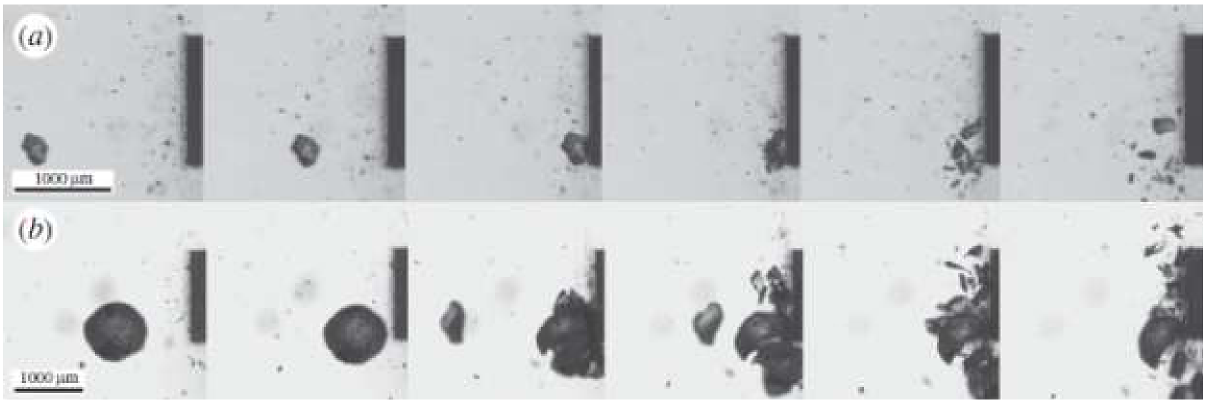

Figure 3: Major fragmentation mode impact of non-spherical (aq) and spherical Particle (b). Timestep beween single frames is 14.9 µs. (Hauk et al. (2015)

ICI occurs only when the warm substrate on which the ice crystals impact is cooled down sufficiently such that the interface between substrate and ice layer is below the melting temperature. Hence, the problem is a classic conjugate heat transfer problem, in which the heat capacity of, and the heat flux in and out of the substrate must also be accounted for (Schremb et al., 2017). The sequence of ice accretion is therefore as follows. Initially the ice crystals impact a warm surface and may or may not adhere, depending on the LWC (Figure 2). With increasing ice accretion however, the warm surface starts to cool down, since the heat flux is from the substrate to the ice layer. Eventually the interface between the substrate and the ice layer reaches freezing temperature and the ice layer is strongly attached to the surface. However, as the ice layer builds up, the underlying surface is increasing insulated from the cold ambient flow and the interface temperature raises above the melting temperature, resulting in a liquid layer between the substrate and the ice layer. At some extent of melting at the interface, the ice layer can then shed from the surface, depending on the surface shape, the accreted ice shape and the forces exerted by shear or pressure drag on the ice layer. The entire sequence then repeats, starting again with a warm surface.

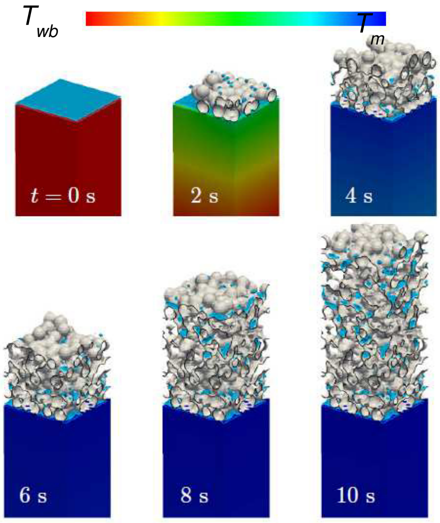

Figure 4: Build up of an ice layer and cooling of the substrate (Kintea et

Such an ice layer build up is pictured in Figure 4. Using a simplified heat transfer model. Kintea et al. (2014, 2016) were able the predict the shedding frequency of an ice layer as measured by Currie et al. (2013). Such a shedding sequence is pictured in Figure 5 in terms of the ice layer thickness.

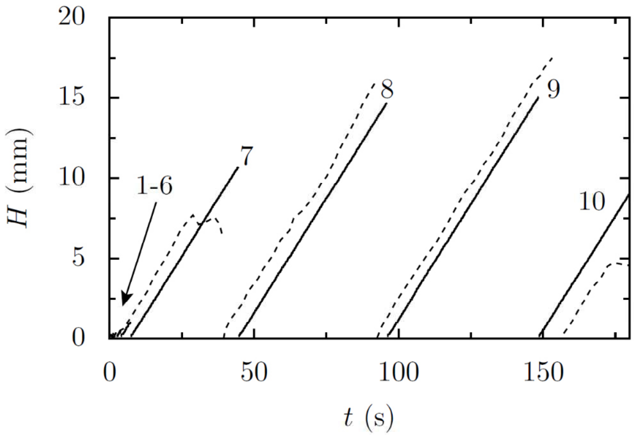

Figure 5: Accretion thickness of run 573 over time. Solid lines correspond to numerical results while dashed lines represent experimental data.

Summary and outlook

This brief survey highlights the numerous fundamental physical phenomena which must be understood in order to reliably model and simulate the accretion of ice from liquid drops and/or ice crystals impacting onto aircraft components. The development of suitable models relies heavily on generic experiments, for one to recognize possible model formulations and second, to serve as validation data for subsequent implementation of the models into prediction codes.

A large number of co-workers must be acknowledged in this report, in particular Dr.-Ing. A. Criscione, M. Gloerfeld M.Sc., Dr.-Ing. Tobias Hauk, Prof. S. Jakirlic, Dr.-Ing. D. Kintea, Prof. I.V. Roisman and Dr.-Ing. M. Schremb. Furthermore, the financial support of the Deutsche Forschungsgemeinschaft (SFB/TRR 75) and the European Union through the projects HAIC, ICE-GENESIS and MUSIC-haic is acknowledged.

References

Criscione, A., I. V. Roisman, S. Jakirlić, and C. Tropea. "Towards modelling of initial and final stages of supercooled water solidification." *International Journal of Thermal Sciences* 92 (2015): 150-161.

Currie, T.C., Fuleki, D., Knezevici, D.C., MacLeod, J.D.: Altitude Scaling of Ice Crystal Accretion, 5th AIAA Atmospheric and Space Environments Conference, San Diego, USA, 2013.

Gloerfeld, Mark, Ilia V. Roisman, Jeanette Hussong, and Cameron Tropea. "Measurements and modelling of the residual mass upon impact of supercooled liquid drops." *Experiments in Fluids* 62, no. 10 (2021): 1-11.

Hauk, T., E. Bonaccurso, I. V. Roisman, and C. Tropea. "Ice crystal impact onto a dry solid wall. Particle fragmentation." *Proceedings of the Royal Society A: Mathematical, Physical and Engineering Sciences* 471, no. 2181 (2015): 20150399.

Kintea, D. M., I. V. Roisman, and C. Tropea. "Transport processes in a wet granular ice layer: Model for ice accretion and shedding." *International Journal of Heat and Mass Transfer* 97 (2016): 461-472.

Kintea, Daniel M., Markus Schremb, Ilia V. Roisman, and Cameron Tropea. "Numerical investigation of ice particle accretion on heated surfaces with application to aircraft engines." In *11th AIAA/ASME Joint Thermophysics and Heat Transfer Conference*, p. 2820. 2014.

Kintea, Daniel M., Tobias Hauk, Ilia V. Roisman, and Cameron Tropea. "Shape evolution of a melting nonspherical particle." *Physical Review E* 92, no. 3 (2015): 033012.

Löwe, Jens, Daniel Kintea, Arne Baumert, Stephan Bansmer, Ilia V. Roisman, and Cameron Tropea. "Inception of ice accretion by ice crystal impact." In *Journal of Physics: Conference Series*, vol. 745, no. 3, p. 032013. IOP Publishing, 2016.

Reitter, L. M., H. Lohmann, M. Schremb, I. V. Roisman, J. Hussong, and C. Tropea. "Impact of an ice particle onto a dry rigid substrate: Dynamic sintering of a residual ice cone." *Cold Regions Science and Technology* 194 (2022): 103416.

Roisman, I. V., and C. Tropea. "Impact of a crushing ice particle onto a dry solid wall." *Proceedings of the Royal Society A: Mathematical, Physical and Engineering Sciences* 471, no. 2183 (2015): 20150525.

Schremb, Markus, and Cameron Tropea. "Solidification of supercooled water in the vicinity of a solid wall." *Physical review E* 94, no. 5 (2016): 052804.

Schremb, Markus, Ilia V. Roisman, and Cameron Tropea. "Transient effects in ice nucleation of a water drop impacting onto a cold substrate." *Physical Review E* 95, no. 2 (2017): 022805.

Schremb, Markus, Ilia V. Roisman, and Cameron Tropea. "Normal impact of supercooled water drops onto a smooth ice surface: experiments and modelling." *Journal of Fluid Mechanics* 835 (2018): 1087-1107.

Schremb, Markus, James M. Campbell, Hugo K. Christenson, and Cameron Tropea. "Ice layer spreading along a solid substrate during solidification of supercooled water: Experiments and modeling." *Langmuir* 33, no. 19 (2017): 4870-4877.

Schremb, Markus, Sven Borchert, Edin Berberovic, Suad Jakirlic, Ilia V. Roisman, and Cameron Tropea. "Computational modelling of flow and conjugate heat transfer of a drop impacting onto a cold wall." *International Journal of Heat and Mass Transfer* 109 (2017): 971-980.

Villedieu, Philippe, Pierre Trontin, Gilles Aouizerate, Stephan Bansmer, Paolo Vanacore, Ilia Roisman, and Cameron Tropea. "MUSIC-Haic: 3D multidisciplinary tools for the simulation of in-flight icing due to high altitude ice crystals." *SAE International journal of advances and current practices in mobility* (2019).

Puffing and micro-explosions in composite droplets: recent modelling results

S.S. Sazhin*[1], D.V. Antonov[2], P.A. Strizhak[2], G. Castanet[3], E.A. Shchepakina[4],
V.A. Sobolev[4], T. Bar-Kohany[5,6]
[1]Advanced Engineering Centre, School of Architecture, Technology and Engineering,
University of Brighton, Brighton, BN2 4GJ, UK
[2]National Research Tomsk Polytechnic University 30, Lenin Avenue, Tomsk 634050, Russia
[3]Université de Lorraine, CNRS-UMR7563, CS 25233, France
[4]Samara National Research University, 34, Moskovskoye Shosse, Samara, 443086, Russia
[5]School of Mechanical Engineering, Tel Aviv University, Tel Aviv, Israel
[6]Department of Mechanical Engineering, nrcn, Israel
*Corresponding author: S.Sazhin@brighton.ac.uk

Introduction

The abstract focuses on the most recent results obtained mainly after publication of [1,2]. These include modelling of puffing/micro-explosion in multi-component composite droplets, arrays of two and three droplets, and the results of our development of the shift model considering the effects of the shift of the location of water sub-droplet from the centre of the fuel droplet.

Multi-component composite droplets

A model of puffing/micro-explosion of multi-component composite water/fuel droplets, developed in [3], uses the same assumptions as the model described in [4] except that the effects of the multi-component nature of the fuel were considered. As in [4], it was assumed that a water sub-droplet is in the centre of a spherical fuel droplet. Assuming that the liquid diffusion coefficient is constant for all species at each time step, the component diffusion equation inside the droplets was solved analytically. In this solution it was considered that fuel components do not penetrate water. Raoult's law was used at the surface of the fuel droplet. The relative diffusion of individual species in the gas phase was not considered. The analytical solution to the component diffusion equation in the liquid phase was incorporated into the numerical code alongside the previously obtained analytical solution for the distribution of temperature inside the droplets. Both solutions were used at each time step of the calculation.

Strings of two and three closely spaced droplets

The results of experimental and theoretical investigation of the mutual effects of two and three composite fuel/water droplets, one behind the other, on their puffing/micro-explosion are presented and discussed in [5,6]. The case of two closely spaced composite rapeseed oil/water droplets in tandem was considered in [5], while [6] was focused on three Diesel fuel/water droplets. In both cases, the effect of interaction between droplets was taken into account via modifications to the Nusselt (Nu) and Sherwood (Sh) numbers for these droplets. The focus of [6] was not only on finding the time to puffing/micro-explosion, but also on the investigation of time evolution of temperature at the fuel-water interface before the development of puffing/micro-explosion.

Shift model

At pointed out in [7] the model developed in [4] and generalised in several later papers summarised in the previous sections has several important weaknesses. (1) the verification of the model was limited by the development of two separate numerical codes, using Wolfram Mathematica v 12.1 and Matlab R2020a, in which the analytical solution to the heat transfer equation in a composite droplet was implemented. Although these codes predicted the same results, both results could be wrong if there are issues with the analytical solution. (2) the sensitivity of the results to the shifting of the water sub-droplet location away from the centre of the fuel droplet was not investigated. (3) no quantitative estimates of the effect of this shift on predicted and observed times to puffing/micro-explosion were made. All these three issues were addressed by the authors of [7]. The predictions of the model described in [4] were verified based on their comparison with the predictions of a numerical code for solving the same heat transfer problem in the fuel-water droplet in which the analytical solution to the heat transfer equation in a fuel-water droplet is replaced with its numerical solution. The latter code was generalised to consider a shift of the water sub-droplet away from the centre of the fuel droplet. This generalisation (called the

Shift Model (SM)) was based on the numerical solution to the heat transfer equation in a fuel-water droplet. The heat transfer equation in this case was rewritten in the cylindrical coordinate system (*r, ϑ, z*), with the *z*-axis being the line joining the centre of the fuel droplet to that of the water sub-droplet. The main simplifying assumption used in the SM is that the surface temperature of the fuel droplet is uniform although it can change with time. The non-uniform spatial distribution of the heat flux at the droplet surface is required to maintain a uniform temperature at the fuel droplet surface.

Acknowledgments

The authors are grateful for the financial support received from the Tomsk Polytechnic University (TPU) development program, Priority 2030 (Priority-2030-NIP/EB-038-1308-2022) which supported S.S. Sazhin (who contributed to the preparation of the text of the paper), D. Antonov (who performed the experiments and contributed to the analysis of the results), and P.A. Strizhak (who contributed to the preparation of the experiments and the analysis of the results), Russian Science Foundation (Grant 21-19-00876), which supported E.A. Shchepakina, and V.A. Sobolev (who contributed to the development of the models), the Universite de Lorraine and the Institut Carnot Icéel for the CALICO (Combustion d'Aérosols LIquides Complexes) grant which supported G. Castanet (who contributed to the development of the models and simulations).

References

[1] Sazhin, S.S., Bar-Kohany, T., Nissar, Z., Antonov, D, Strizhak, P., and Rybdylova, O., 2021, Proceedings of the 15th Triennial International Conference on Liquid Atomization and Spray Systems. Edinburgh, UK, 29 Aug.-2 Sept. 2021. Paper 18.

[2] Sazhin, S.S., 2022, “Droplets and Sprays: Simple Models of Complex Processes” Springer (series ‘Mathematical Engineering’).

[3] Sazhin, S.S., Shchepakina, E., Sobolev, V.A., Antonov, D.V., and Strizhak, P.A., 2022, Int. J Heat Mass Transfer, 184, 122210.

[4] Sazhin, S.S., Bar-Kohany, T., Nissar, Z., Antonov, D., and Strizhak, P.A., 2020, Int. J Heat Mass Transfer, 161, 120238.

[5] Antonov, D.V., Fedorenko, R.M., Strizhak, P.A., Castanet, G., and Sazhin, S.S., 2021, Int. J Heat Mass Transfer, 176, 121449.

[6] Antonov, D.V., Volkov, R.S., Fedorenko, R.M., Strizhak, P.A., Castanet, G., and Sazhin, S.S., 2021, Int. J Heat Mass Transfer, 181, 121837.

[7] Castanet, G., Antonov, D.V., Strizhak, P.A., and Sazhin, S.S., 2022, Int. J Heat Mass Transfer, 186, 122466.

Twin Background Subtraction: a Simultaneous Thermographic Measure of Thickness and Temperature of a Liquid Film

R. Clavenna, L. Araneo*, A. Salerno
Politecnico di Milano, Energy Department, Milano, Italy
*Corresponding author: lucio.araneo@polimi.it

Introduction

The development of techniques to measure the thickness and the temperature of a liquid film is an interesting topic for many two-phase flow studies. Various methods based on different physical principles have been proposed in the literature depending on the range of thickness investigated, fluid properties, wall material, and interface properties, many of them are able to measure the two properties by independent techniques or instruments [1, 2], more rarely by the same instrument [3]. We present here an original technique aimed at measuring the temperature and the thickness of a film, by a unique thermographic imaging device with a relatively simple set-up.

Methods

The novel technique is based on non-invasive optical, infrared measurement, and is named Twin Background Subtraction (TBS). The technique allows the simultaneous measurement of the temperature and of the thickness of a thin film optically accessible through two infrared transparent sapphire windows. The maximum thickness measurable depends on the attenuation coefficient of the fluid for the particular IR wavelengths investigated [4]. In the tested set-up, water is used as fluid, and a mid-wave IR camera (Flir Titanium 3.6-5.1µm) is used to obtains two different images. Each image is composed partially by the emission from the investigated film, and partially by a different background whose emission is attenuated by the same film positioned in-between the background and the camera. The signal S received by the IR camera is usually proportional to the surface temperature fourth power of an opaque body, leading to a measured temperature T_M. In the present configuration, the following simplified equations can be used to quantify and manipulate the received signal as a function of the film and windows temperatures T_F and T_W and of the used background temperatures T_{B1} or T_{B2}, leading to two different signals S_1 and S_2. Note that the IR camera software would report directly two measured temperatures T_{M1} and T_{M2}.

$$\begin{cases} S_1 = \varepsilon_1 T_{B1}^4 \cdot \tau_F \tau_w^2 + \varepsilon_w T_F^4 \cdot \tau_F \tau_w + \varepsilon_F T_F^4 \cdot \tau_w + \varepsilon_w T_F^4 = T_{M1}^4 \\ S_2 = \varepsilon_2 T_{B2}^4 \cdot \tau_F \tau_w^2 + \varepsilon_w T_F^4 \cdot \tau_F \tau_w + \varepsilon_F T_F^4 \cdot \tau_w + \varepsilon_w T_F^4 = T_{M2}^4 \end{cases}$$

Some simplifications and assumption are used.

The film temperature is constant along its thickness, or an equivalent average is used.

Reflections are neglected, so that for both film and windows the transmission and emission coefficients are equal ($\tau=\varepsilon$). Each signal S_1 or S_2, is composed by: the emission from the corresponding background attenuated by the passag through the film and both sapphire windows (these terms will be named B_1 and B_2), the emission from the back window attenuated by the film and the front window, the emission from the film attenuated by the front window, and the emission from the front window. Each emission is expressed as a function of the emitter temperature and emissivity coefficient ε, The background temperature is imposed, its emissivity is chosen as close as possible to 1; both windows reach quite rapidly the film temperature, that is also imposed; the window attenuation, and therefore emissivity, can be easily measured.

As a first approximation, Beer-Lambert law correlating the film transmissivity with its thickness L_F is written with an average linear attenuation coefficient b_F fitted in the used wavelength range film thickness L_F and expected temperature. More complex expressions may be used with more terms, to better fit the real attenuation dependent on the wavelength.

$$\tau_F = \epsilon_F = exp(-b_F \cdot L_F)$$

With the aforementioned hypotheses and simplifications, the solution of the system of equations gives the film temperature T_F and the film transmissivity τ_F ; the latter, thanks to Beer-Lambert law, is used to estimate the film thickness.

$$B_1 = \varepsilon_1 T_{B1}^4 \cdot \tau_F \tau_w^2 \qquad B_2 = \varepsilon_2 T_{B2}^4 \cdot \tau_F \tau_w^2$$

$$\begin{cases} L_F = \frac{-1}{b_F} \cdot ln \frac{S_2 - S_1}{B_2 - B_1} \cdot \frac{1}{\tau_w^2} \\ T_F^4 = \frac{S_1 - B_1 \cdot \tau_F \tau_w^2}{\varepsilon_F \tau_w + \varepsilon_w (1 + \tau_F \tau_w)} \end{cases}$$

The first equation solving L_F shows that the emission terms from the film and the windows are cleared away when subtracting the two signals, so that the signal difference (S_2-S_1) is equal to the background difference (B_2-B_1), attenuated by the film and the windows, independently from the film emission. So the measured background difference attenuation gives directly the film thickness, like it happens in usual attenuation based measurement techniques not disturbed by film emission.

Note that the signal expression S contains two unknowns, T_F and τ_F (or L_F), and to solve for them two different equations are necessary. In the present discussion, the different equaltions are obtained by using two background temperature T_B, but a difference may be obtained as well by changing another parameter, like exploiting the different emission and attenuation in two different bandwidths characterized by sufficiently different attenuation coefficients b_F, while keeping the same background.

Experimental set-up

An experimental set-up was developed to test the TBS technique. The scheme is reported in the exploded view of Figure 1. The IR camera is on the left. The film to be measured, represented in green, has the shape of a square wedge, and is formed by the water contained between two square sapphire windows 40*40mm^2, here depicted in grey and shown slightly separated. The two backgrounds beyond the film can be easily translated on a transversal rail to switch them; they consist of commercial cold plates, black painted, with two circuits feeding them with water at the chosen temperatures T_{B1} and T_{B2}, represented by the blue and red colours. Figure 2 shows the details of the sapphire window support; one window can be slightly tilted to change the top thickness of the wedge shaped film included. The two sapphire windows resulted to be slightly convex, so the wedge shows a slightly concavity of about 40 µm; the film thickness can range between 0 to 500 µm. A fluid circuit provides the film water at the chosen temperature T_F.

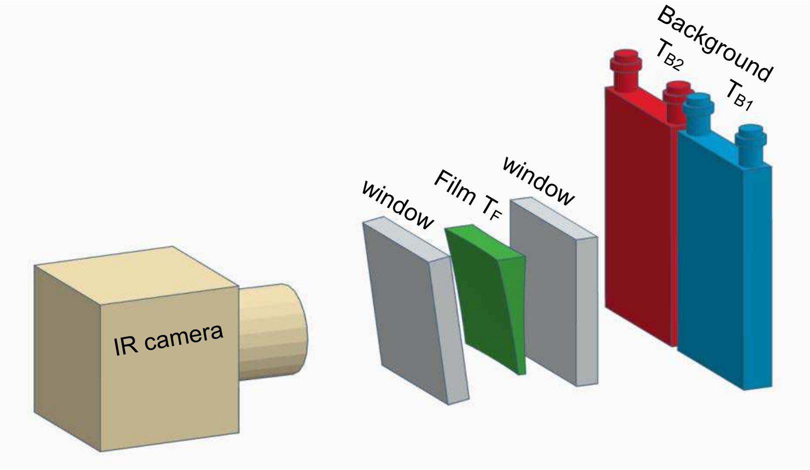

Figure 1. Scheme of the TBS set-up

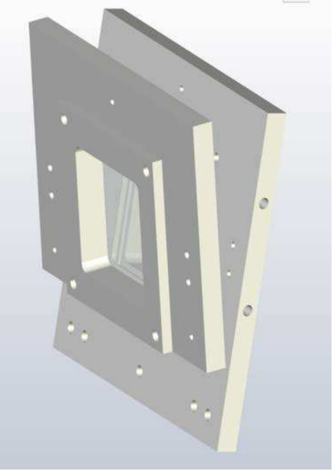

Figure 2. The window support.

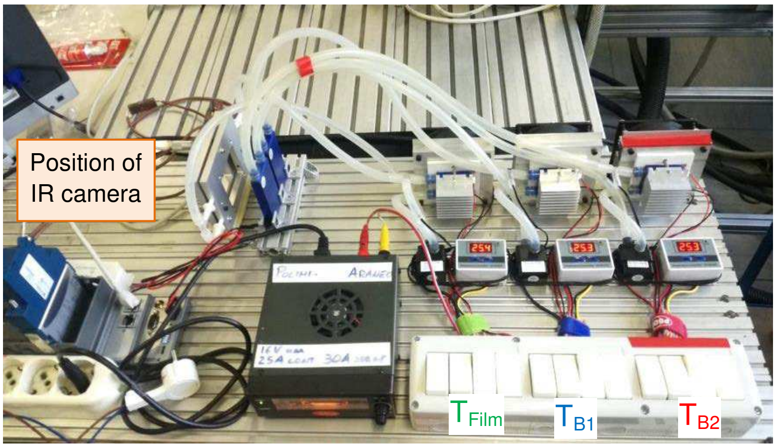

Figure 3. The TBS set-up with the fluid circuits

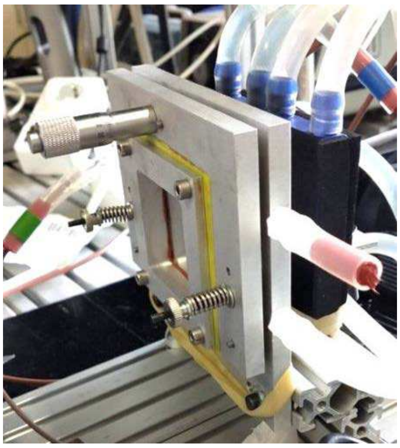

Figure 4. The real window support.

All the fluid circuits can be cooled or heated at the chosen temperatures by a system of Peltier cells; the fluid temperatures are also measured after each device to control the temperature values and stability. The experiments were performed keeping the film temperature at a constant value between 15 to 50°C, with the two backgrounds at constant temperatures T_{B1}=15°C and T_{B2}=45°C.

Results and Discussion

The results from three test are reported as examples in figures 5 to 7. Each figure reports the result as 3D plots of the measured thickness and temperature as functions of the XY coordinates, corresponding to the 40*40 mm^2 window visualized with a resolution of 100*100 pixel^2.

Figure 5 shows the results for T_F=15°C, with 100 μm of distance on one edge of the windows, the minimum is reached where the two windows get in contact due to their convexity. Around the contact region, where the film is very thin, both temperature and thickness results show high variation, or impossible results, due to the experimental errors leading to null denominator or negative logarithm arguments. Where the film is thicker than 10÷20 μm, the measured thickness and temperatures gives more realistic results.

Figure 6 shows the results for T_F=25°C, and parallel windows, with 100 μm of distance on the edges, and about 60 μm at the concavity. In this case all measurements are corresponding to the reality, showing good accuracy and very fine precision.

Figure 7 shows the results for T_F=45°C, with the wedge changing from 100 to 500 μm of distance. The thickness results are accurate up to 300 μm, then the attenuation is too high and noise dominates, due most probably to the too low bit resolution of the IR images, together with the reduced relative accuracy. On the contrary the temperature measures are nearly perfect, since the film becomes so thick that can be considered fully opaque, the residual signals from the background become negligible.

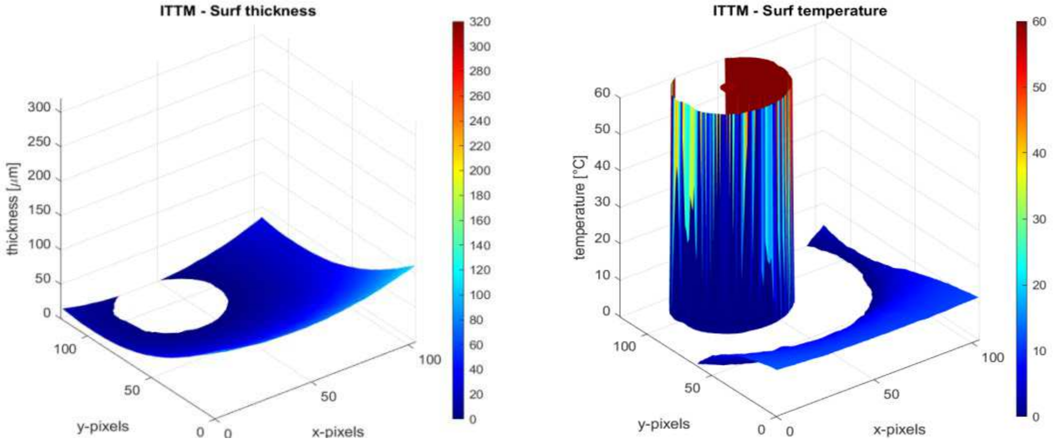

Figure 5. Measured thickness and temperature distribution, wedge range 0-100 μm, TF=15°C

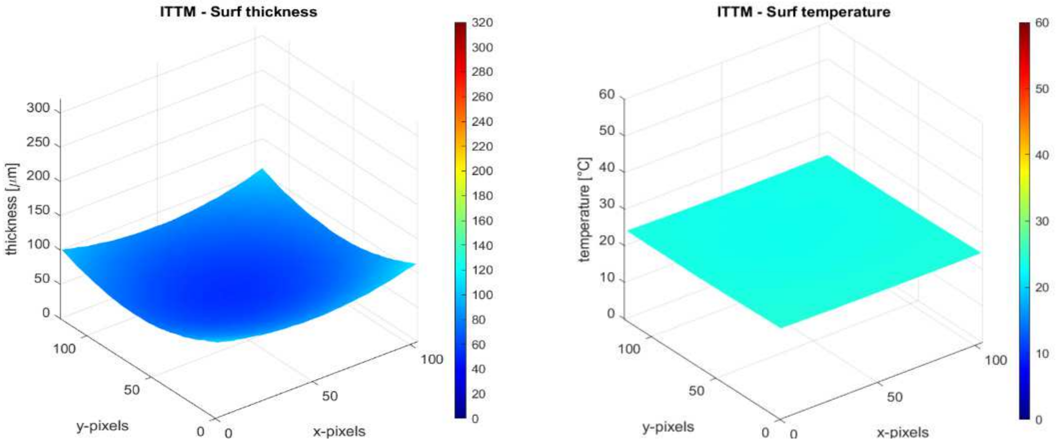

Figure 6. Measured thickness and temperature distribution, wedge range 60-100 μm, TF=25°C

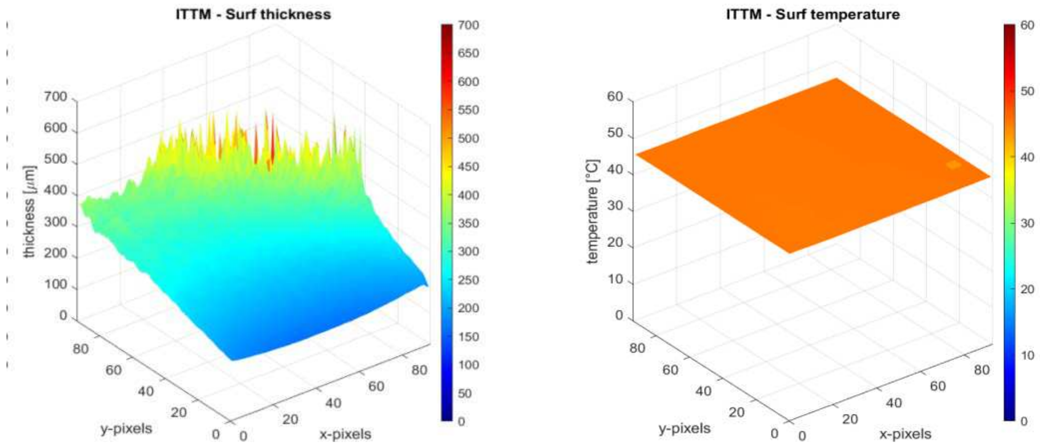

Figure 7. Measured thickness and temperature distribution, wedge range 100-500 µm, TF=45°C

Future development of the technique are aiming at measuring simultaneously the temperature and thickness of the liquid film around a vapour bubble in a capillary tube. The simultaneity of the two images is obtained as shown in figure 8 with a single camera thanks to the use of a mirror and to the symmetry of the system.

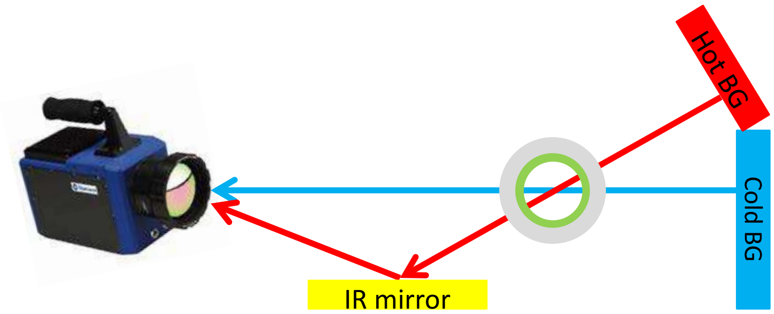

Figure 8. Set-up for measurements of the liquid layer around a bubble in a capillary tube.

The technique can be adapted with different configurations. The use of two cameras allows the simultaneous view of the same target from two inclinations, or from opposite sides. A patterned background with spots or lines at different temperatures, or emissivity, allows the use of a single image. The film laying on a mirror surface would double the active thickness increasing the accuracy for thin films. Fast IR led may be used to illuminate differently the background. The principle used may be extended to two components fluids to measure the concentration of one component in the form of solution or dispersions.

Conclusion

A novel technique named TBS, Twin Background Subtraction, has been proposed and successfully tested. It is able to measure the temperature and thickness of an IR semi-transparent film in the range of thickness where the film shows an attenuation that is not negligible nor too close to total, in the used infra-red bandwidth. When tested with water the technique shows promising accuracy in the range of 10-300µm, with a precision that could make it complementary to traditional optic techniques more suited for thicker films.

The technique can be exploited with different configurations, and is promising for the study of optically thin films, both solid or liquid, like in multiphase flows involving film evaporation or condensation.

Acknowledgements

The present work is carried forward in the framework of the project "Two-Phase Passive Thermal Devices For Deployable Space Systems (TOPDESS)", financed through the Microgravity Application Program (MAP N. 4000128640) by the European Space Agency.

References

[1] Bigonha Tibiriçá, C., do Nascimento, F. J., Ribatski, G., Exp. Therm. Fluid Sci., 34, 2010.
[2] Dupont, J., Mignot, G., Paladino, D. and Prasser, H. M., Nucl. Eng. Des., 336, 2018.
[3] Wu, W., Kong, S., Xu, X, Tao, J, Li, C, Wang, J, Su, M, Yang, H., Spectrochim. Acta A, 257, 2021
[4] Limbaugh C., The Infrared Emission-Absorption Method for Temperature and Species Partial Pressure Determination in Flames and Plumes, in *Infrared Methods for Gaseous Measurements*,1985 ISBN 0824774299

Drops retracting while forming a rim

Y. Stern[1], V. Multanen[1], A. Vinod[1], R. Tadmor[1]*
[1]Ben Gurion University of the Negev, Department of Mechanical Engineering,
tadmorr@bgu.ac.il

Introduction

Surfactant laden droplets may spread faster on a substrate and, subsequently, retract (spontaneously reversing the drop's direction) [1-8]. We hypothesize that this Marmur-Lelah type retraction can be explained using a de Gennes-type triple line fluctuation expression [9-12] that is modified to represent our anisotropic surfactant adsorption. This explanation requires that the retraction originates inner to the triple line (not at the triple line itself). As a result of retraction emanating from a location inner to the triple line, a rim is formed as the drop retracts, as shown in Fig. 1. The formation of this rim, as well as its behavior should be dependent on the concentration of surfactant in the drop. Furthermore, these should be more prominent at low surfactant concentrations, hence this study investigates low surfactant concentrations on the spreading-retraction system.

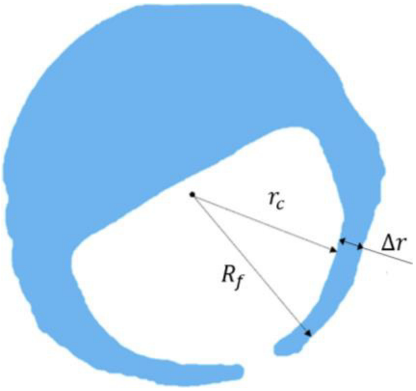

Figure 1. Representation of rim formation upon retraction via a shadow image of a drop. In this case, the drop is a tetradecane oil drop with octadecylamine as the surfactant. The solid substrate is mica. In the figure, we have some key quantities: R_f is the final base radius at the end of spreading, r_c is the critical radius from which retraction commences, and $\Delta r = R_f - r_c$ is the eventual width of the rim upon retraction. We will see how Δr depends on concentration in the discussion section.

Materials and methods

Octadecylamine (ODA) (Sigma, Israel, Purity $\geq 99\%$) was added to tetradecane (TD) (Sigma, Israel, Purity $\geq 99\%$) and mixed at room temperature. Several ODA concentrations were tested, while here we report representative results for the cases of $0.6\ mM$ and $1.2\ mM$. Mica surfaces (S&J Trading Inc., USA) were cleaved in a laminar flow hood cabinet with a HEPA filter. Droplets of $4\ \mu L$ of the ODA/TD solution were dispensed on the freshly cleaved mica surfaces inside the laminar hood and the spreading and retracting processes were observes using a Nikon 1 J5 digital camera equipped with 1 Nikkor VR 30-110 lens and two stacked Movo EXT- NM47 autofocus extension tubes. The footage was processed with Adobe Premiere Pro CC 2020 software.

The spreading angle for the ODA/TD system is considered to be $\theta_{sp} = 8°$, although the system never quite reaches this angle before retraction [8,10]. The post-retraction contact angle is $\theta_{RT} = 39°$. The surfactant adsorption is that of monolayer adsorption [13]. We measured the surface tension of the ODA/TD solution at $\gamma_{LV} = 26\ \frac{mJ}{m^2}$ which is equal to that of pure TD, showing that ODA is not active at the liquid-vapor interface. However, we will show that it is active at the solid-vapor interface and is in fact what drives retraction.

Results and discussion

While retraction of ODA/TD at high surfactant concentration may sometimes be isotropic, in the case of low concentrations none of the dozens of experiments we ran were isotropic. Figs. 2 and 3 demonstrate this fact, as well as demonstrating the formation of a rim at low concentrations. It should be noted that this is a non-volatile system, so unlike some previous studies which found that evaporation causes retraction [14] we show that it is not necessary.

We now explain why this happens. Upon the end of the spreading phase, the drop is still while fluctuations occur near the triple line. To cause retraction, a fluctuation must expose enough of a lower surface-energy region of the substrate such that it is energetically favorable for a further inward intrusion to take place. Based on a criterion originally posed by de Gennes [9], we obtain that [15]

$$\frac{\Delta\gamma}{\gamma_{LV}}\Delta r^2 > 10k_BT \qquad (1)$$

Where $\Delta\gamma$ is the difference between the solid-vapor surface energy of the bare substrate and that of the substrate after the adsorption of the surfactant on it. It should be noted that $\Delta\gamma$ is not only time-dependent but also depends on the radial position due to the initial spreading of the drop. Additionally, Δr is the inward progression of the fluctuation, and k_BT is the thermal energy. In other words, we require a large enough surface energy difference with a critical intrusion that goes deep enough in order to cause retraction.

At higher surfactant concentrations, $\Delta\gamma$ is much higher and therefore the intrusion does not need to be very deep in order to cause retraction. Therefore, in such cases retraction occurs virtually from the triple line itself (or rather, at a point extremely close to it) and therefore a visible rim is not observed.

On the other hand, at low surfactant concentrations, an intrusion must go relatively deep in order to cause retraction due to the fact that $\Delta\gamma$ is not as large. Therefore, in these cases we obtain a visible rim which becomes wider as surfactant concentration decreases. This is seen in Figs. 2 and 3, where the $0.6\,mM$ ODA/TD drop had a significantly wider rim than the $1.2\,mM$ drop.

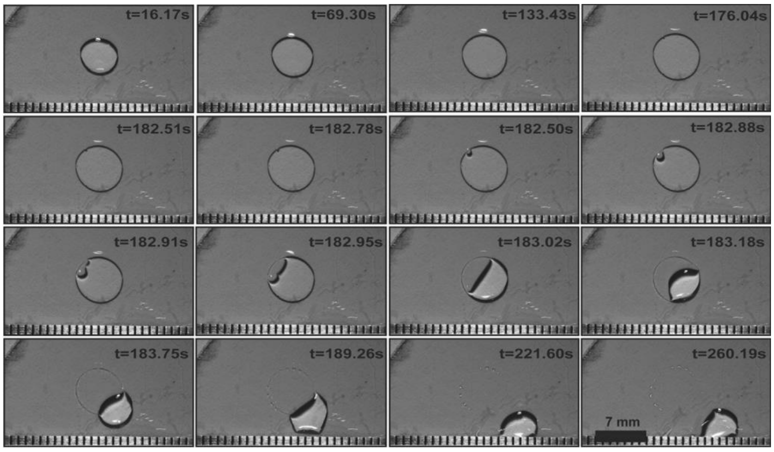

Figure 2. Experimental results of ODA/TD for a $4\,\mu L$ drop with $1.2\,mM$ ODA concentration. Ambient conditions are $23\,°C$ and 50% relative humidity.

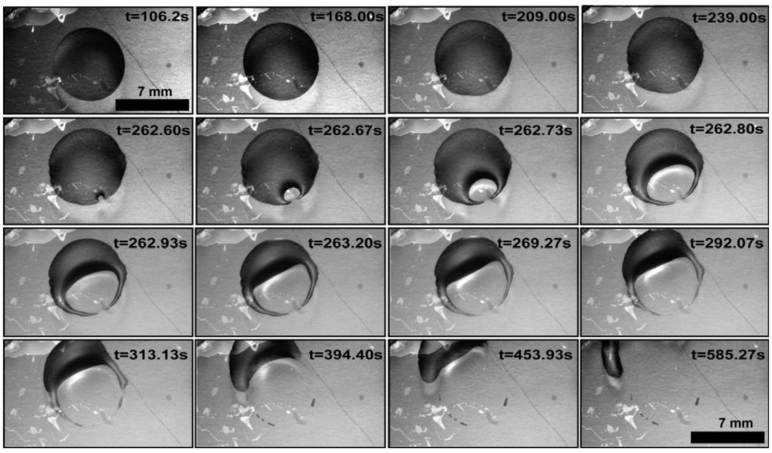

Figure 3. Experimental results of ODA/TD for a $4\,\mu L$ drop with $0.6\,mM$ ODA concentration. Ambient conditions are $23\,°C$ and 50% relative humidity.

As can be seen in the above figures, the lower surfactant concentration developed a wider rim. In addition, we also see a qualitative difference in the behavior of the rim between the two cases. At the $1.2\,mM$ concentration, the rim stays behind and eventually breaks up into smaller droplets, while at $0.6\,mM$ the rim gets sucked back into the retracting drop. This difference can be explained by a simple balance of the force on the rim due to the Laplace pressure difference between it and the bulk drop against surface viscous drag forces. In other words, as the rim gets wider the Laplace pressure difference dominates the drag forces while for thinner rims the drag force is too high such that the rim stays behind and eventually breaks up into droplets.

Finally, by observing the frames corresponding to the spreading phase in Figs. 2 and 3, a plot of the base radius against time can be built. This plot serves to corroborate Tanner's law of spreading [16], which can be stated as

$$\frac{R}{R_f} = \left(\frac{t}{t_f}\right)^n \tag{2}$$

Where R is the base radius, R_f is the final/maximal base radius, t is time and t_f is the time at which spreading ends. Now, as shown in Fig. 4 we find a good for Tanner's law with $n \approx 0.1$ for both concentrations.

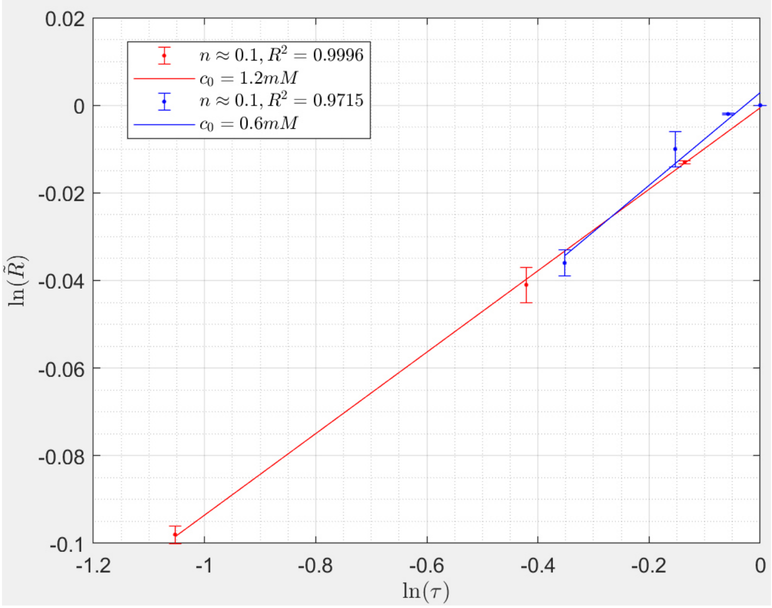

Figure 4. Validation of Tanner's law, where across both concentrations a log-log plot of the base radius against time provides a slope of $n \approx 0.1$.

Note that in the above figure, we use the dimensionless parameters $\tilde{R} = \frac{R}{R_f}, \tau = \frac{t}{t_f}$.

Ultimately, in this work we have demonstrated the formation of a rim at low surfactant concentrations and have particularly demonstrated this due to the retraction of a non-volatile droplet. We provide a theory which explains the size and behavior of the rim depending on the surfactant concentration, as well as experimental evidence for this theory. Finally, we corroborate Tanner's law of spreading for the spreading phase.

Nomenclature

R_f	Final/maximal spreading radius
r_c	Critical radius from which retraction occurs
Δr	Rim width/critical intrusion depth for retraction
θ_{sp}	Equilibrium spreading contact angle
θ_{RT}	Equilibrium retraction contact angle
γ_{LV}	Liquid-vapor surface tension
$\Delta\gamma$	Solid-vapor surface energy difference between initial (bare) substrate and substrate upon adsorption of surfactant
$k_B T$	Thermal energy
R	Base radius (depends on time)
t	Time
t_f	Final time of spreading

References

[1] A. Marmur, M. Lelah, The spreading of aqueous surfactant solutions on glass, Chem. Eng. Commun. 13 (1981) 133–143.

[2] S. Troian, X.L. Wu, S.A. Safran, Fingering instability in thin wetting films, Phys. Rev. Lett. 62 (1989) 1496.

[3] A. Marmur, Equilibrium and spreading of liquids on solid surfaces, Advanc. in Coll. and Interf. Sci 19 (1983) 75–102.

[4] M. Ghosh, K.J. Stebe, Spreading and retraction as a function of drop size, Advanc. in Coll. and Interf. Sci 161 (2010) 61–76.

[5] H. Greenspan, On the motion of a small viscous droplet that wets a surface, J. Fluid Mech 84 (1978) 125–143.

[6] X. Fang, B. Li, E. Petersen, Y. Ji, J.C. Sokolov, M.H. Rafailovich, Factors controlling the drop evaporation constant, J. Phys. Chem. B 109 (2005) 20554–20557.

[7] R. Tadmor, Drops that pull themselves up, Surf. Sci. 628 (2014) 17–20.

[8] R. Tadmor, A. Baksi, S. Gulec, S. Jadhav, H. E N'guessan, K. Sen, V. Somasi, M. Tadmor, P. Wasnik, S Yadav. Drops that change their mind: spontaneous reversal from spreading to retraction. Langmuir 35 (2019) 15734-15738.

[9] P.G. de Gennes, F. Brochard-Wyart, D. Quere, Capillarity and Wetting Phenomena Drops, Bubbles, Pearls, Waves, Springer-Verlag, New York, 2003.

[10] R. Tadmor, A. Baksi, S. Gulec, et al., Defying gravity: drops that climb up a vertical wall of their own accord, J. Colloid Interf. Sci 562 (2020) 608–613.

[11] H. Wang, R.J. Composto, Kinetics of surface and interfacial fluctuations in phase separating polymer blend films, Macromolecules 35 (2002) 2799–2809.

[12] J. Rodríguez-Hernández, C. Drummond, Polymer Surfaces in Motion: Unconventional Patterning Methods, Springer International Publishing, Switzerland, 2015.

[13] R. Tadmor, R.E. Rosensweig, J. Frey, J. Klein, Resolving the puzzle of ferrofluid dispersants, Langmuir 16 (2000) 9117–9120.

[14] X. Zhong, F. Duan, Dewetting transition induced by surfactants in sessile droplets at the early evaporation stage, Soft Matter 12 (2016) 508–513.

[15] R. Tadmor, V. Multanen, Y. Stern, Y.B. Yakir. Drops retracting while forming a rim. J. Colloid Interface Sci. 581 (2021) 496-503.

[16] L.H. Tanner. The spreading of silicone oil drops on horizontal surfaces. J. Phys. D: Appl. Phys. 12 (1979) 1473-1484.

Narrow Band-Based Dynamic Load Balancing for Multiphase Flow Simulation

D. Appel*[1], J. Zeifang[2], A. Beck[3]
[1] Institute of Aerodynamics and Gas Dynamics, University of Stuttgart, Germany
[2] Institute of Fluid Dynamics and Thermodynamics, University of Magdeburg, Germany
[3] Computational Mathematics, Hasselt University, Belgium
*Corresponding author: daniel.appel@iag.uni-stuttgart.de

Introduction

One of the major challenges to the efficient utilization of HPC systems is load balance, i.e. the even distribution of the application workload across the processor units. Temporal changes in the workload at runtime, in particular, necessitate a dynamic load balancing approach. In general, these workload variations can on the one hand be inherent to the numerical scheme, as with adaptive spatial grids or local time stepping techniques. On the other hand, they may arise from coupling different physical models to describe multiscale problems like particulate flows or direct hybrid aeroaccoustics.

The present report is based on our previous work in [1] and proposes a dynamic load balancing approach for space-filling curves (SFCs), with application to multiphase flow simulations using the Level-Set Ghost-Fluid method. The Level-Set Ghost-Fluid method was first suggested by Fedkiv et al. [2] and has since been improved by many authors, recently by Jöns et al. [3] for a high-order framework. As sharp-interface method, it regards the two phases as immiscible fluids which are separated by an interface Γ of zero thickness. The location of the interface is given by the root of the level-set function $\phi(\boldsymbol{x})$, from which geometrical quantities like the interface normal $\boldsymbol{n}$ and the curvature κ can directly be inferred. The motion of the interface is described by the transport equation

$$\phi_t + s \cdot \nabla\phi = 0. \qquad (1)$$

with the transport velocity s. The latter emerges from the two-phase Riemann problem and is extrapolated from the interface into the volume by solving the Hamilton-Jacobi equation [4]

$$s_\tau^d + \operatorname{sign}(\phi)\, \boldsymbol{n} \cdot \nabla s^d = 0. \qquad (2)$$

Here, the superscript indicates the velocity component along dimension $d = 1,2,3$, and τ denotes the pseudo time. Since the signed-distance property of the level-set function is not preserved by the transport equation (1), it needs to be restored regularly by solving the additional Hamilton-Jacobi equation [5]

$$\phi_\tau + \operatorname{sign}(\phi)\,(|\nabla\phi| - 1) = 0. \qquad (3)$$

As the information of the level-set field is only of interest near the interface, the preceding three equations are only solved in its close vicinity, termed narrow band [6]. In consequence, the computational domain $\mathcal{D}$ can be decomposed into three intersecting sets of grid cells [1]: the bulk elements $\mathcal{D}_{\text{bulk}} \equiv \mathcal{D}$ that discretize the Euler equations, the narrow band elements $\mathcal{D}_{\text{NB}} \subset \mathcal{D}_{\text{bulk}}$ in which additionally the three level-set equations (1)-(3) are solved, and the elements containing the phase interface, $\mathcal{D}_\Gamma \subset \mathcal{D}_{\text{NB}}$, subject to the calculation of the curvature and the two-phase Riemann problem. The computational costs of a singular grid cell rises in the listed order of these subsets. In parallelized computations, this cost hierarchy naturally implies an uneven workload distribution, which additionally varies in time due to the interface dynamics.

Dynamic Load Balancing

The outlined framework operates on unstructured, curved grids. Hence, also Cartesian grids as the ones shown below are internally represented as an unstructured mesh. For the domain decomposition, it employs a Hilbert space-filling curve (SFC). In terms of dynamic load balancing, SFCs conveniently reduce the d-dimensional partitioning problem to one dimension by translating the spatial workload distribution of N grid cells into a task chain of positive weights w_i with $i = 1, \dots, N$. Partitioning algorithms for SFCs seek to decompose this task chain into P consecutive segments such that the bottleneck value, i.e. the maximum workload among all P processors, is minimized. Formally, the bottleneck value is defined as

$$B = \max_{i \le p \le P} \{W_p\} \qquad (4)$$

with the processor (or partition) workload

$$W_p = \sum_{j=s_{p-1}+1}^{s_p} w_j \tag{5}$$

and s_p denoting the index of the last task assigned to processor p. Given the weight vector $(w_1, \dots, w_N)$ of the current workload distribution, the partitioning algorithm thus determines the sequence of optimal separator indices $s_0 = 0 \leq s_1 \leq \cdots \leq s_P = N$. An ideal partitioning would only have identical processor workloads, resulting in the so-called ideal bottleneck

$$B^* = \frac{1}{P}\sum_{i}^{N} w_i. \tag{6}$$

Comparing the actual bottleneck to this value permits to assess the quality of the partitioning, which can be expressed in terms of the imbalance

$$I = \max_p\{I_p\} = \max_{\mathrm{p}}\{\frac{W_p}{B^*} - 1\}. \tag{7}$$

In order to determine the current workload distribution, the proposed load balancing scheme performs element-local wall time measurements, which exploit the introduced distinction of three element types. The wall time measurements account for the fact that the costs of these element types depend on the specific simulation setup, for example through the chosen numerical flux function, the discretization of the bulk and level-set equations, and the frequency of invoking the extrapolation and reinitialization procedures, (2) and (3) respectively. From an implementational perspective, the introduced subsets, $\mathcal{D}_{\mathrm{bulk}}$, $\mathcal{D}_{\mathrm{NB}}$ and D_Γ define three element masks that are passed to the bulk and level-set operators. The masks allow to infer the element-local wall times from distributing the operator costs evenly among the masked elements. These element wall times can then readily be used as weights w_i. The suggested approach results in a minimally intrusive code instrumentation with negligible runtime overhead, and avoids any empirical weighting factors.

In practice, the element wall times are measured every nth time step, where $n = \mathcal{O}(10^2)$ needs to be adjusted to the dynamics of the workload variations in the considered setup. Upon exceeding a threshold, $I > I_{\mathrm{th}}$, the evaluated imbalance triggers the actual repartitioning and the subsequent redistribution of the grid cells among the processors. Figure 1 illustrates the working principle of the outlined load balancing scheme for a two-dimensional droplet resting in a quiescent gas, based on a representative grid resolution and solver setup.

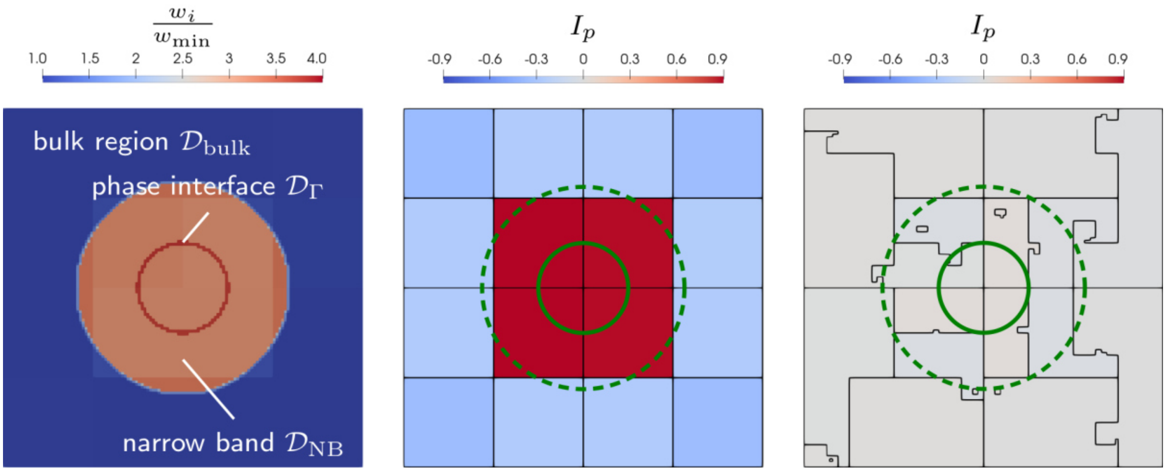

Figure 1. Domain decomposition for $P = 16$ processors for a two-dimensional droplet resting in quiescent gas: Dimensionless element wall times (left), processor imbalances before (middle) and after repartitioning (right), with a overall workload imbalance of $I = 0.921$ and $I = 0.023$, respectively (adopted from [1]).

Results and Discussion

In order to assess the performance gain achieved through the presented load balancing scheme, we compare the strong scaling behavior of balanced and unbalanced simulations. The investigated test case essentially extends the setup of Figure 1 to three dimensions, where stationary physics allow us to isolate the effect of the repartitioning. We use two different grid resolutions, corresponding to a discretization of 50 and 100 DOFs per diameter, and a problem size of 16.7M and 134M DOFs in total, respectively. All runs were performed on the HPE Apollo System *HAWK* at the High Performance Center Stuttgart and cover a range of up to 131072 processors. The system is equipped with 5632 compute nodes, each with two 64-core AMD EPYC 7742 CPUs and 256GB

RAM, and deploys the InfiniBand HDR200 interconnect with a bandwith of 200GBit/s for the internode communication. As a performance metric, we analyze the performance index PID, which measures the wall time required by a single core to advance one DOF for one stage of the RK time integration scheme

$$\mathrm{PID} = \frac{\text{total runtime } \times \#\text{cores } P}{\#\text{DOFs} \times \#\text{time steps} \times \#\text{RK-stages}}. \tag{8}$$

Additionally, we evaluate the parallel efficiency η, which relates the obtained PID to that of a single compute node

$$\eta = \frac{\mathrm{PID}_{P=128}}{\mathrm{PID}} \in [0{,}1]. \tag{9}$$

Figure 2 shows a speed-up of up to factor 10 for the balanced simulations, while reaching a parallel efficiency of 86% on average, compared to 29% for the unbalanced simulations.

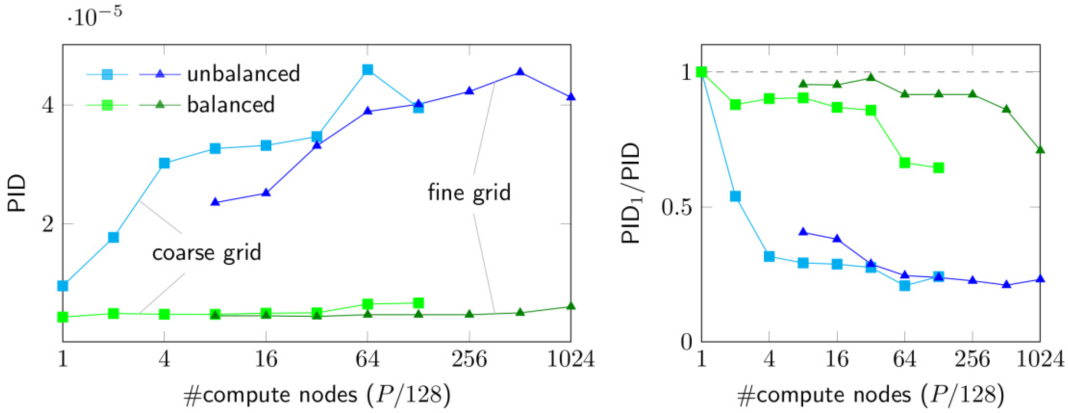

Figure 2. Strong scaling behavior for a three-dimensional droplet resting in quiescent gas.

The reported performance gain also carries over to more complex and realistic scenarios that feature dynamic workload variations. As an example, we revisited the shock-drop interaction studied by Jöns et al. [3] and Winter et al. [7]. Specifically, we considered the Rayleigh-Taylor piercing (RTP) regime where aerodynamic forces are relatively small compared to surface tension forces, resulting in the characteristic bag breakup. For details on the setup and the physics, the reader is referred to the cited work. In this simulation, the dynamic load balancing scheme provided an overall runtime reduction of 87% and 92% for 2D and 3D setup, respectively.

Finally, we shift the focus on the partitioning algorithm itself. Various algorithms have been proposed over the years, but comprehensive comparisons are rare, especially with real simulation data and today's large processor counts. We investigated established heuristics as well as recently published algorithms, using the element weights of the above shock-drop interaction as input data. Our primary quality metric was the load balance

$$Q = \frac{B_{\mathrm{opt}}}{B} \in [0{,}1] \tag{9}$$

with $Q = 1$ indicating the optimal workload distribution. This definition accounts for the fact that the ideal bottleneck B^* is usually not feasible due to the discrete nature of the element weights. The lowest feasible bottleneck, by contrast, is referred to as optimal bottleneck B_{opt} and can often be achieved with more than one partitioning. Algorithms that always return an optimal partitioning are called exact, opposed to heuristics.

One of the earliest inexact algorithms is the popular H2 heuristic by Miguet and Pierson [8], which for each partition independently determines the separator index closest to the ideal one, and is thus fast and parallelizable. The heuristic used by the presented multiphase framework was adopted from the PICLas framework [9] and incorporates this idea into a probing-based algorithm, that tries to find a partitioning with B smaller than an iteratively adjusted limit. Among the exact algorithms is the recently published version of exact bisection by Lieber and Nagel [10], termed ExactBS+PI. We also include their HIER algorithm in our comparison, which combines H2 and ExactBS+PI in a hierarchical, parallelizable ansatz to efficiently provide near-exact partitionings. Moreover, we take into account the heuristic by Niemöller et al. [11], that incrementally minimizes the imbalance by shifting the partition separators individually with the aim of controlling the task migration.

Task migration itself is defined as the relative share of tasks that the partitioning algorithms assigns to a different processor than before

$$\mathrm{TM} = \frac{N_{\mathrm{migrated}}}{N} \in [0{,}1] \tag{10}$$

Since for the simulation, this migration implies exchanging element data via communication operations, TM indicates the induced cost of the repartitioning.

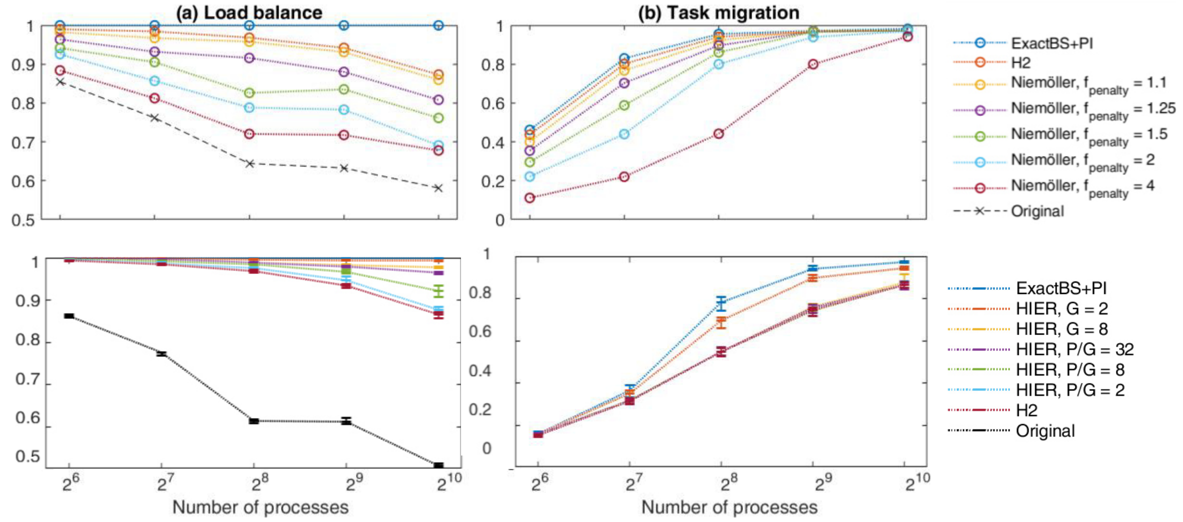

Figure 3. Strong scaling behavior of load balance Q and task migration TM for various partitioning algorithms, using the workload distribution of the 2D simulation of a shock-drop interaction simulation in [1] as input data.

Figure 3 depicts the strong scaling behavior of both metrics, Q and TM, for the aforementioned partitioning algorithms. The two upper plots compare the algorithm of Niemöller et al. [11] to H2 and ExactBS+PI. As expected, ExactBS+PI reaches the optimal load balance, $Q = 1$, but also causes the highest task migration. To reduce the task migration, the algorithm incorporates a parameter that penalizes shifts of the partition separators. Increasing this penalty factor indeed reduces TM, however at the expense of Q. The HIER algorithm as well offers a free parameter that controls the influence of H2 versus ExactBS+PI, which is reflected by the above scaling curves. The currently employed heuristic [9] usually outperforms H2 in terms of Q and TM at similarly fast execution times (not shown). While in the present case, ExactBS+PI proves to be the most suitable algorithm, this choice generally remains a trade-off between fast execution times and high-quality partitionings.

References

[1] D. Appel, S. Jöns, C. Müller, J. Zeifang and C.-D. Munz, "A narrow band-based dynamic load balancing scheme for the level-set ghost-fluid method," in *High Performance Computing in Science and Engineering '21 (in press)*, 2021.

[2] R. Fedkiv, T. Aslam, B. Merriman and S. Osher, "A non-oscillatory Eulerian approach to interfaces in multimaterial flows (the ghost fluid method)," *Journal of Computational Physics,* vol. 152, no. 2, pp. 457-492, 1999.

[3] S. Jöns, C. Müller and J. Zeifang, "Recent advances and complex applications of the compressible ghost-fluid method," *Recent Advances in Numerical Methods for Hyperbolic PDE Systems,* vol. 28, pp. 155-176, 2021.

[4] T. Aslam, "A partial differential equation approach to multidimensional extrapolation," *Journal of Computational Physics,* vol. 193, no. 1, pp. 349-355, 2004.

[5] M. Sussman, P. Smereka and S. Osher, "A level set approach for computing solutions to incompressible two-phase flow," *Journal of Computational Physics,* vol. 114, no. 1, pp. 146-159, 1994.

[6] D. Peng, B. Merriman, S. Osher, H. Zhao and M. Kang, "A PDE-based fast local level set method," *Journal of Computational Physics,* vol. 155, no. 2, pp. 410-438, 1999.

[7] J. Winter, J. Kaiser, S. Adami and N. Adams, "Numerical investigation of 3d drop-breakup mechanisms using a sharp interface level-set method," in *11th International Symposium on Turbulence and Shear Flow Phenomena*, Southhampton, 2019.

[8] S. Miguet and J.-M. Pierson, "Heuristics for 1d rectilinear partitioning as a low cost and high quality answer to dynamic load balancing," in *International Conference on High-Performance Computing and Networking*, Vienna, 1997.

[9] S. Fasoulas, C.-D. Munz, M. Pfeiffer, J. Beyer, T. Binder, S. Copplestone, A. Mirza, P. Nizenkov, P. Ortwein and W. Reschke, "Combining particle-in-cell and direct simulation Monte Carlo for the simulation of reactive plasma flows," *Physics of Fluids,* vol. 31, 2019.

[10] M. Lieber and W. Nagel, "Highly scalable SFC-based dynamic load balancing and its application to atmospheric modeling," *Future Generation Computer Systems,* vol. 82, pp. 575-590, 2018.

[11] A. Niemöller, M. Schlottke-Lakemper, M. Meinke and W. Schröder, "Dynamic load balancing for direct-coupled multiphysics simulations," *Computers & Fluids,* vol. 109, 2020.

Effect of edge length and surface wettability on droplet impact onto a macroscopic surface structure

A. K. Geppert*, P. Foltyn, B. Weigand
Institute of Aerospace Thermodynamics, University of Stuttgart, Germany
*Corresponding author: anne.geppert@itlr.uni-stuttgart.de

Introduction

Droplet impact on dry, structured surfaces is ubiquitous in technological applications, e.g., in spray painting, self-cleaning surfaces or cooling of micro-electronic devices. These applications also depend on the wetting behavior of the surface. Spray painting requires a high wettability of the surface to achieve an even distribution of the paint, while self-cleaning surfaces repel liquids due to their very low surface wettability. The performance of micro-electronic devices strongly depends on the efficient control of the emerging thermal loads. The most promising cooling technology for this task is the surface engineering-enhanced spray cooling [1]. Here, the targeted engineering of surface wettability and structure can increase the efficiency of the spray cooling. However, the physical mechanisms involved are quite complex and therefore no clear design principles are available. Thus to improve spray cooling efficiency and to meet the different demands of the other technologies, a better understanding of the complex interplay between surfaces structure and wettability is needed.

To achieve this, a simplified test case is defined in which a single droplet impacts onto a stand-alone cubic pillar with varying surface wettability. To begin with, we performed a combined numerical/experimental study of the impact process on a cubic pillar with an edge length of 1 mm, whose surface satisfied full wetting conditions [2]. The study showed a very good agreement between the droplet impact morphologies and unraveled the process of air entrapment underneath the droplet, which can lead to bubble formation. The latter would reduce the heat transfer capability of the pillar surface strongly. In a second step, we extended the drop impact investigation by varying the edge length of the cubic pillar between 1 mm and 2.4 mm as well as its surface wettability (fully wetting, partly wetting, and hydrophobic). The obtained results are summarized in the following.

Experimental Parameters and Multi-Perspective Experimental Facility

The droplet impact process is visualized with a multi-perspective experimental facility [3]. It records the droplet impact process from three time-synchronous perspectives simultaneously, namely top, side and bottom view (see Fig. 1). The top and side view employ the classical diffuse backlight imaging or shadowgraphy technique. Note that, the top view is recorded at an angle of 13.4° to avoid obstructing the droplets' falling trajectory. The bottom view uses the total internal reflection method [4, 5] that allows to distinguish dry and wetted surface areas and thus to track the liquid-solid contact area (see Fig 1). Figure 1a,e show the fourth perspective, which records a three-dimensional impression of the impact scenery. In Foltyn et al. [3] detailed information on the facility and the post-processing procedures can be found. The image acquisition is triggered when the falling droplet passes a laser light barrier. Liquid accumulation and regular dripping off at the tip of a tilted needle generates the droplets. Their diameter varies between 2 mm (isopropanol) and 2.4 mm (distilled water) depending on the chosen fluid. The impact velocities of 1.5 m/s and 2.4 m/s are achieved by adjusting the droplets falling height. Hence, the investigated parameter variation also includes multiple droplet diameters, impact velocities and two fluids, namely distilled water and isopropanol. The surface specimen, i.e. the cubic pillars, are made of acrylic glass. The wetting behavior of the surface specimen was manipulated using plasma activation to achieve a high surface wettability and contact angles of $\theta \approx 0°$ and plasma polymerization to get a reduced surface wettability at contact angles of $\theta \approx 70°$. The investigation encompasses in total 65 experiments. Here, only the results for droplet impacts close to the pillar center are considered, while off-center impacts are excluded.

Results and Discussion

In a first step, we discuss the effect of pillar size and wettability on the impact morphology. If the pillar edge length is much smaller than the diameter of the impacting droplet, ground spreading occurs. This is characterized by the droplet liquid flowing around the pillar, enclosing it and finally spreading out along the surrounding substrate, as shown in Figure 1b-d. The spreading is uniform in all directions, which leads to a circular shape of the liquid lamella. The bottom view, employing the total internal reflection method, confirms the liquid spreading along the solid substrate. At first sight, this would be a preferable spreading condition for a cooling process. However, during the spreading of the liquid, air is entrapped at the pillar side faces and corners [4]. Subsequently, air bubbles form,

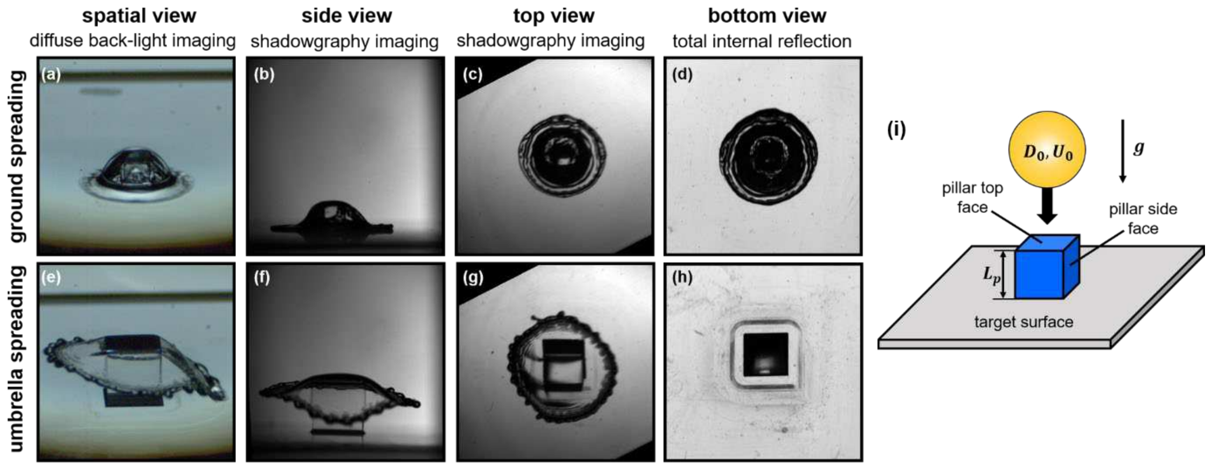

Figure 1. Images captured with the multi-perspective experimental facility. The upper row shows ground spreading at t = 4 ms (pillar size: 1 mm; droplet size: 2.4 mm, droplet velocity: 2.4 m/s) from a) spatial view, b) side view, c) top view and d) bottom view perspective. The lower row depicts umbrella spreading at t = 3.6 ms (pillar size: 2.4 mm; droplet size: 2.4 mm, droplet velocity: 2.4 m/s) from e) spatial view, f) side view, g) top view and h) bottom view perspective. Subfigure i) shows the droplet impact problem schematically.

which are completely separated from the pillar sides. How these air bubbles might affect a cooling process needs to be further investigated. If the droplet diameter is in the same order or larger than the pillar edge length, the impact morphology changes completely. Shortly after impact, the droplet starts to spread on top of the pillar surface and continues to spread in mid-air beyond the edge of the pillars' top surface. This is shown in Figure 1e-g. This behavior is confirmed by the bottom view image in Figure 1h that shows a wetted pillar top, while the surface around the pillar stays completely dry. Only at a later time, the liquid lamella sinks down along the pillar side faces due to gravity and impacts onto the surrounding surface. Thereby, the lamella stretches across the pillar edges and ruptures. We call this impact morphology umbrella spreading. The shape of the lamella observed during umbrella spreading also differs significantly from the one observed during ground spreading. It exhibits a rectangular shape, with the lamella corners azimuthally rotated by 45° with respect to the pillar corners. Juarez et al. [6] observed the same behavior for droplet impacts onto posts with cross-sectional polygon geometries. The size of their posts was in the order of the droplet diameter and impact conditions were similar to ours. Subsequent to the breakup of the lamella rim, they observed the formation of liquid filaments, whose number corresponds to the number of corners of the polygon-shaped post. In our experiments, we also observe the formation of filaments, but on the solid surface around the pillar not in mid-air. Therefore, the filament formation is strongly affect by the surface wettability, while the transition from ground to umbrella spreading is triggered by the ratio of pillar to droplet size. Filament formation is more pronounced for reduced wetting conditions ($\theta \approx 70°$), where the filaments are still visible after the end of the spreading process. On the contrary, for full wetting conditions ($\theta \approx 0°$) a dissolving of the filaments is observed.

The presented results give some new insights into the impact behavior of droplets onto free standing cubic surface structures, but we are still at the beginning of our investigation and the understanding of the complex impact dynamics involved.

References

[1] Xu, R., Wang, G., and Jiang, P., Spray Cooling on Enhanced Surfaces: A Review of the Progress and Mechanisms, ASME. *J. Electron. Packag.*, 144(1): 010802, 2022.

[2] W. Ren, P. Foltyn, A. Geppert, and B. Weigand. Air entrapment and bubble formation during droplet impact onto a single cubic pillar, *Sci. Rep.*, 11(1):18018, 2021.

[3] P. Foltyn, D. Ribeiro, A. Silva, G. Lamanna, and B. Weigand. Influence of wetting behavior on the morphology of droplet impacts onto dry smooth surfaces, *Phys. Fluids*, 33(6):063305, 2021.

[4] N. R. Arnold Frohn. Dynamics of Droplets. Springer Berlin Heidelberg, 2000.

[5] M. A. J. van Limbeek, M. Shirota, P. Sleutel, C. Sun, A. Prosperetti, and D. Lohse. Vapour cooling of poorly conducting hot substrates increases the dynamic Leidenfrost temperature. *Int. J. Heat Mass Transf.*, 97:101-109, 2016.

[6] G. Juarez, T. Gastopoulos, Y. Zhang, M. L. Siegel, and P. E. Arratia. Splash control of drop impacts with geometric targets. *Phys. Rev. E*, 85(026319), 2012.

Numerical Investigation of the Mechanism of early Crown Formation at an oblique Droplet Impact onto a Wall Film

J. Stober*, K. Schulte
Institute of Aerospace Thermodynamics, University of Stuttgart, Germany
*Corresponding author: jonathan.stober@itlr.uni-stuttgart.de

Introduction

In most spray impact scenarios in technical applications, many droplets impact obliquely on the wetted wall. The macroscopic result shows different crown shapes on both sides of the impact point. On the downstream side the crown is bent outwards and thin. In contrast on the upstream side, the crown is bent inwards at early times $(\tau = t\frac{D}{U} < 2)$. This can be seen in Figure 1, which shows the interface at the symmetry plane for the dimensionless times $\tau = 1$ and $\tau = 2$, respectively and has also been observed in literature [1-3].

The mechanisms behind early crown formation during oblique drop impact are not yet fully understood, especially on the upstream side, and have now been investigated more detailed with the use of highly resolved Direct Numerical Simulations.

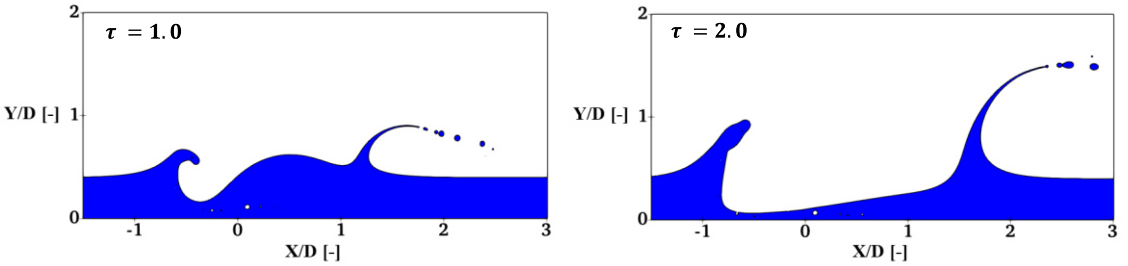

Figure 1. Interface at the symmetry plane at an oblique droplet impact. The droplet impacts from the left and contacts the wall film at position $X/D = 0$. Upstream refers to negative x-position, whereas downstream refers to positive x-position. Dimensionless time $\tau = \frac{t\,D}{U} = 1$ on the left, $\tau = \frac{t\,D}{U} = 2$ on the right.

Numerical Setup

The direct numerical program package Free Surface 3D (FS3D) solves the incompressible Navier-Stokes equations for multi-phase flows using a volume-of-fluid method (VOF), [4]. To reduce computational cost, the symmetry of the problem was exploit and only a half of the geometry was simulated. The domain is shown in Figure 2. The red cuboid marks the area of grid refinement consisting of cubic cells, which grow gradually outwards. The grid consists of 2.7 Billion cells with a resolution of 350 $\mathrm{cells/D}$ within the refinement.

The material properties of Hexadecane and air were used for the liquid and ambient gas, respectively. The droplet has a diameter of $D = 2.4\,mm$ impacting at an angle of $\alpha = 60°$ with a velocity of $U = 3.3\,m/s$. The dimensionless wall film thickness is $\delta = h/D = 0.4$. The commonly used dimensionless parameters Weber number and Ohnesorge number are $We = \rho U^2 D/\sigma = 750$ and $Oh = \mu/\sqrt{\rho\sigma D} = 0.015$, respectively. Furthermore, the dimensionless length X/D, the dimensionless velocity $\tilde{u} = |u|/U$ and the dimensionless time $\tau = t\,D/U$ are used in the following.

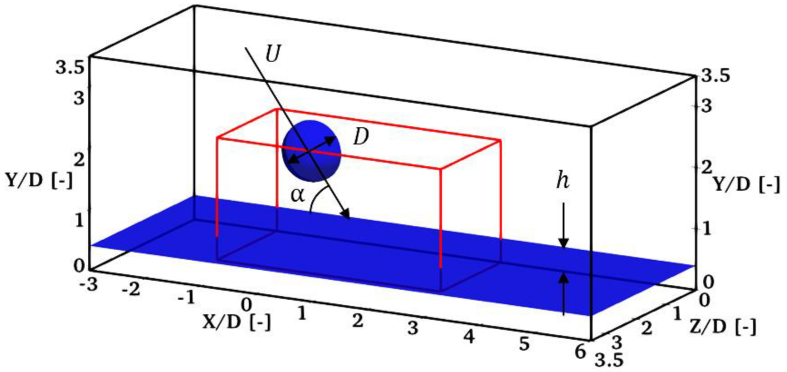

Figure 2. Sketch of the computational domain showing the initial condition and coordinate system.

Figure 3 compares the interface at the dimensionless time $\tau = 0.33$ at the upstream side for three different grid resolutions. The depth of the notch is approximately the same for the two highest resolutions, but increases in thickness with higher resolution. The detachment of a secondary droplet is only captured by the two highest resolutions. It can be said, that full grid convergence is not reached and exact quantities are not reliably resolved. However, the general shape and the phenomenon are qualitatively resolved with 350 cells/D.

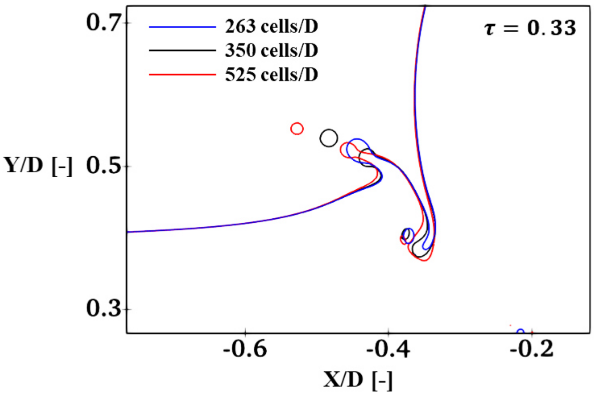

Figure 3. Interface at different resolutions, upstream side.

Results and Discussion

Figure 4 displays the development of the interface and the velocity field in the symmetry plane. On the left side, a zoom to the lamella formation on the upstream side is shown, and on the right to the downstream side.

On the downstream side the process of formation of the lamella is very similar to that at a normal impact. First, at $\tau = 0.08$, there is a high acceleration of a small mass of fluid outwards, which forms the initial lamella. In the subsequent time steps more mass is accelerated to the side and feeds into the horizontally growing lamella, see $\tau = 0.19$ and $\tau = 0.33$. This process continues and the velocity vector at the start of the lamella, and also the direction of the lamella, turns more upwards with increasing time, see $\tau = 0.50$. The oblique impact promotes the ejection of the lamella and crown formation on the downstream side, as also stated by [2] and [3].

Looking at the upstream side the process starts very similar with a high acceleration of a small mass of wall film fluid escaping to the side, $\tau = 0.08$, even though the velocities are little lower. However, shortly after, when the drop penetrates further into the wall film ($\tau = 0.19$), the fluid of the drop is not able to follow the strong deflection necessary to continue feeding into the initial lamella anymore because of the horizontal velocity component in the drop. The fluid is still deflected sideward and upwards, but with a larger radius of deflection. This process continues and ambient air, which is dragged by the impacting drop, penetrates into the wall film and forms a notch, see $\tau = 0.33$. At this time one secondary droplet detaches from the initial lamella formed at $\tau = 0.08$. This initial lamella recedes back into the new thick lamella which is formed by the notch and the upwards deflected fluid, see $\tau = 0.33$ and $\tau = 0.50$. At the upstream side of the drop impact the ejection of a lamella is inhibited. Nevertheless, a crown is formed from a different mechanism leading to a thicker and lower crown bending inwards.

Future Work

One subject still open for future work is the influence of the impact angle α. This will definitely change the mechanism of lamella ejection. The impact angle α has to fall below a critical angle α_c in order for the described mechanism to occur. This α_c could be determined and investigated in future. Another question is how the formation of the lamella changes in azimuthal direction φ. Also, here there could be a critical azimuth angle φ_c where the lamella formation changes from one mechanism to the other.

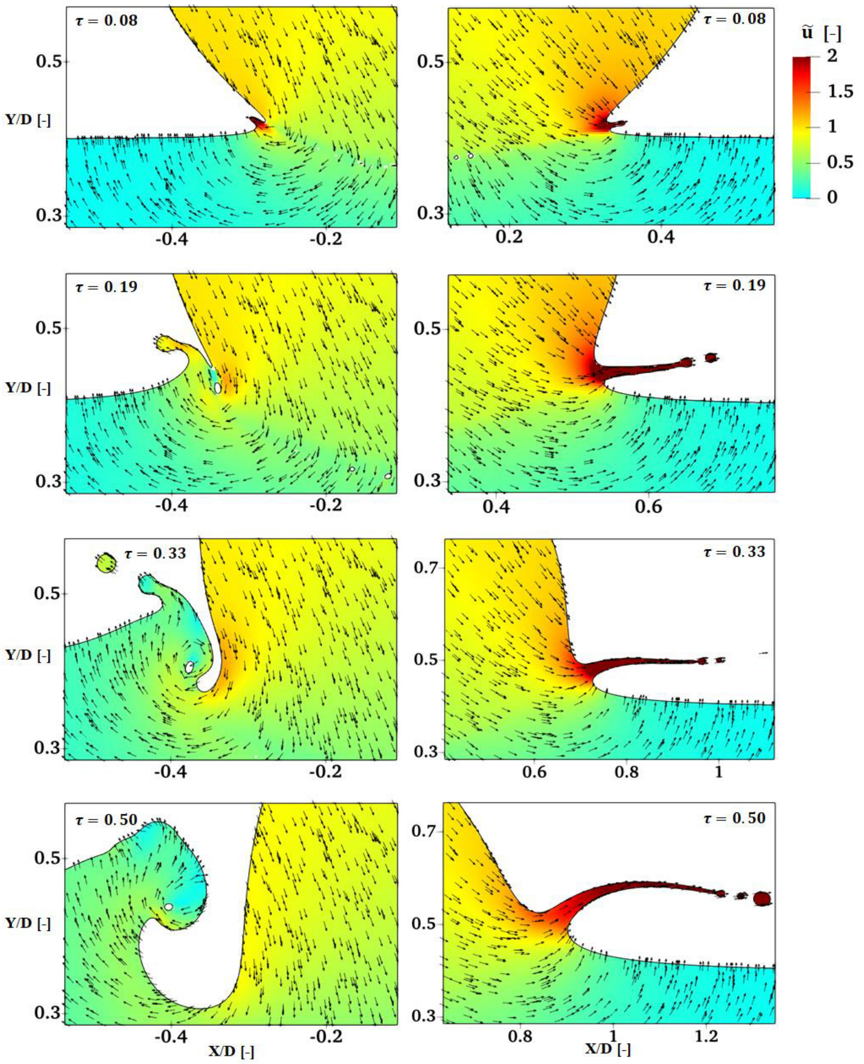

Figure 4. Development of the interface and velocity field on both sides of the impact point at the symmetry plane. Zoom on upstream side (left) and downstream side (right). Same scale for the dimensionless velocity $\tilde{u} = |u|/U$ for all dimensionless times $\tau = t\ D/U$.

Nomenclature

D	initial droplet diameter [m]
h	initial wall film thickness [m]
Oh	Ohnesorge number [-]
t	time [s]
U	initial droplet velocity [m/s]
u	velocity vector [m/s]
$\tilde{u}$	dimensionless velocity [-]
We	Weber number [-]
α	impact angle [°]
δ	dimensionless wall film thickness [-]
μ	dynamic viscosity [kg/(m s)]
ρ	density [kg/m³]
σ	surface tension [N/m]
τ	dimensionless time [-]

References

[1] Brambilla, P., Guardone, A., Assessment of dynamic adaptive grids in Volume-Of-Fluid simulations of oblique drop impacts onto liquid films, Journal of Computational and Applied Mathematics 281: 277-283 (2015)
[2] Guo, Y., Lian, Y., High-speed oblique drop impact on thin liquid films, Phys. Fluids 29, 082108 (2017)
[3] Chen, Z., Shu, C., Wang, Y., Oblique drop impact on thin film: Splashing dynamics at moderate impingement angles, Phys. Fluids 32, 033303 (2020)
[4] Eisenschmidt, K., Ertl, M., Gomaa, H., Kieffer-Roth, C., Meister, C., Rauschenberger, P., Reitzle, M., Schlottke, K., Weigand, B., Appl Math and Comp, 272-2: 508-517 (2016)

Dynamic Contact Angle Measurements of Droplets Spreading on Surfaces of Varying Wettability

P. Palmetshofer*[1], P.Foltyn[1], A. Geppert[1], B. Weigand[1]
Insititute of Aerospace Thermodynamics, University of Stuttgart, Germany
*Corresponding author: Patrick.palmetshofer@itlr.uni-stuttgart.de

Introduction

The contact angle of a liquid on a surface plays an important role in many applications where liquid flows interact with solids. While rough estimates often suffice, precise knowledge of the interface behavior is required in others. Recently, advances in computing power and numerical methods have made it possible to predict many small-scale and medium-scale phenomena featuring multiphase flows. The methods used, however, often only feature a crude implementation of the contact angle. To verify contact angle models, precise data on the spreading behavior of liquids on surfaces is required.

Thus, in this work, the dynamic contact angles of droplets deposited onto smooth surfaces are measured.

Methods

Diffuse backlight imaging/shadowgraphy was used to generate images of droplets spreading on smooth Polymethylacrylate (PMMA) surfaces. Two different experimental setups were used. A DataPhysics Optical Contour Analysis (OCA) device was modified to obtain medium framerate measurements. The low framerate camera was substituted for a KronTech Chronos 1.4 camera. Videos were recorded at 1,057 frames per second with a resolution of 1280 x 1024 pixel².

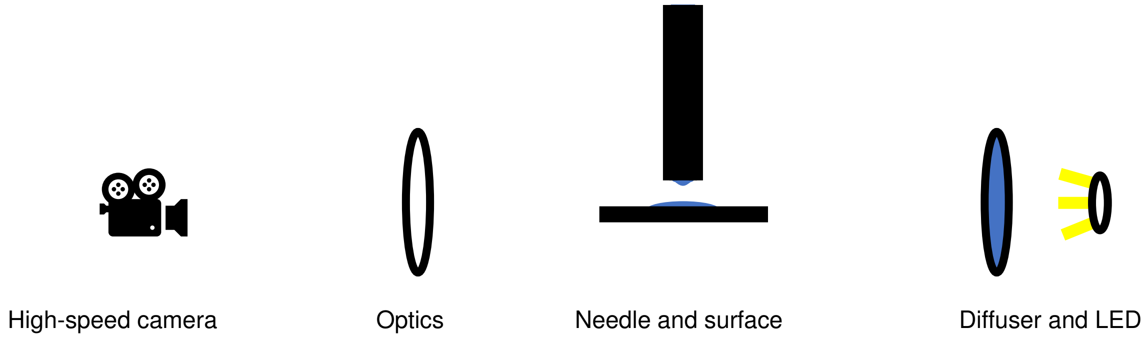

Figure 1. Schematic showing the experimental setups

A second setup was used to obtain measurements at a higher framerate of 20,000 frames per second at a resolution of 1024 x 672 pixel² using a Photron SA-X2 camera.

For the evaluation of the contact angles, the MATLAB library of Nis [1] was used. After image processing, the code was used to evaluate the medium framerate cases, using the reflection of the droplet at the surface to fit the baseline. In the high framerate cases, no reflection was visible. Thus, the baseline points were manually selected from a single image in each experiment. In both cases, the polynomial fitting method was used to determine the contour of the droplet in the vicinity of the surface. The MATLAB code determines the contact angle as the angle at the intersection point between the fitted curve and the baseline.

The fluids investigated in this study were pure distilled water, isopropanol (>99 %) and various polymethylsiloxane silicone oils with different viscosities. These were used to study the effect of the viscosity independent of other fluid parameters. The properties of the liquids are stated in table 1.

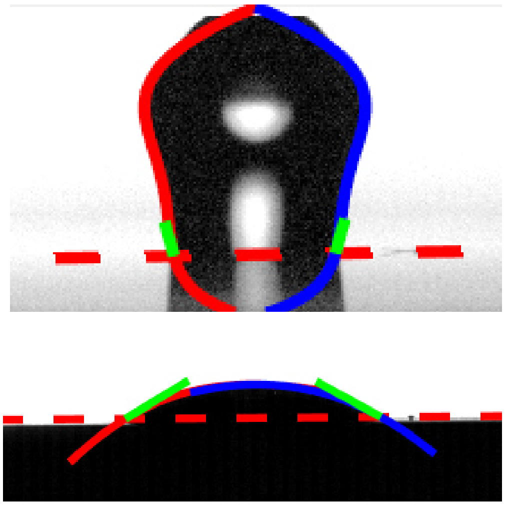

Figure 2. Curve fits for the apparent contact angle

Results

The results show that even in cases that feature an asymptotic behavior early in the development of the apparent contact angle, an overshoot of the contact angle can occur. In some cases, the timing of this overshoot is shifted with respect to other experiments. This is most likely due to the minor differences in the needle location during the detachment process.

While all experiments using B10 show strongly damped behavior the contact angle of water on PMMA is a weakly damped oscillation, resulting from a combination of a high contact angle of water on PMMA, the high surface tension and low viscosity of water. Notably, the regular oscillation does not start before approximately 0.01 s into the process. This time is the time it takes for the droplet to spread while at later times the location of the three-phase contact line stays relatively fixed on the surface.

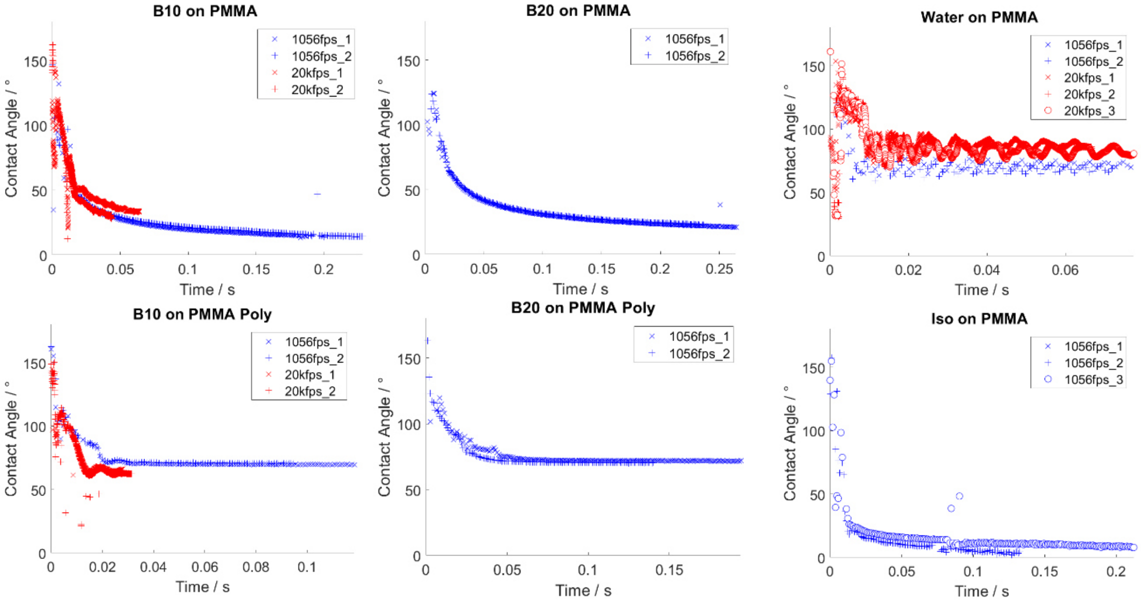

Figure 1. Sample cases for silicone oil, isopropanol and water droplets on treated and untreated PMMA surfaces with high and low framerate imaging cases

Outlook

In the future, methods to generate non-oscillating, but free-falling droplets at very low impact velocities need to be found to make it possible to consistently achieve the same pre-impact conditions. This would greatly increase the comparability between experiments, especially between high- and low-framerate measurements. Additionally, as soon as our in-house code FS3D features a stable implementation of a contact angle model, the results of experiments like those presented in this study have to be compared to the computational calculations.

Acknowledgments

This work was funded and supported by the German Research Foundation/Deutsche Forschungsgemeinschaft (DFG) in the scope of the International Research Training Group/Graduiertenkolleg "Droplet Interaction Technologies" (GRK 2160/2: DROPIT)

References

[1] Nis (2022). Drop shape analysis. Fit contact angle by double ellipses or polynomials (https://www.mathworks.com/matlabcentral/fileexchange/57919-drop-shape-analysis-fit-contact-angle-by-double-ellipses-or-polynomials), MATLAB Central File Exchange. Retrieved June 16, 2022.

A model of droplet evaporation: a new mathematical development

S. Tonini[1], G.E. Cossali[1], E.A. Shchepakina[2], V.A. Sobolev[2], S.S. Sazhin*[3]
[1]Department of Engineering and Applied Sciences, Università degli Studi di Bergamo, Viale Marconi 5, 24044 Dalmine (BG), Italy
[2]Samara National Research University, 34, Moskovskoye Shosse, Samara, 443086, Russia
[3]Advanced Engineering Centre, School of Architecture, Technology and Engineering, University of Brighton, Brighton, BN2 4GJ, UK
*Corresponding author: S.Sazhin@brighton.ac.uk

Introduction

The importance of the problem of modelling droplet evaporation is well known and has been widely discussed [1,2]. A rigorous approach to this problem based on the solution to the heat and mass transfer equations inside and outside droplets, taking into account arbitrary droplet shape and the contributions of other droplets in the system, is out of the question for realistic engineering applications [1,2]. This approach would be unrealistic and unnecessary for the analysis of real-life sprays, that include millions of droplets, which has stimulated the development of many simplified models of the relevant processes.

The most widely used such model is the one developed by Fuchs and Spalding and later refined by Abramzon and Sirignano [2]. This model, widely known as the Abramzon and Sirignano model, however, is based on a number of assumptions the applicability of which to realistic sprays is not at first obvious (see the detailed analysis of this model in [2]). Perhaps the most important of these assumptions is the assumption that the density of the mixture of vapour and ambient air does not depend on the distance from the droplet surface.

The authors of [3] developed a model without using this assumption. Although the model described in [3] does not lead to an explicit formula for the evaporation rate, as in the case of the Abramzon and Sirignano model, the suggested algorithm for finding this evaporation rate is much simpler than the one which would be required if a rigorous model were used. This simplicity was achieved by retaining only the leading term in the asymptotic expansion of the equation for the vapour mass fraction. The reasons for doing this, however, were not fully investigated and justified. The aim of this abstract, which summarises the results presented in [4], is to revisit the model developed in [3] using much more rigorous mathematical analysis of the problem based on the tools developed for the asymptotical analysis of the underlying equations [5].

Analysis

The analysis is based on steady-state mass, momentum and energy balance equations for the vapour and air mixture surrounding a droplet. The previously obtained solution to these equations was based on the assumption that the parameter ε (proportional to the squared ratio of the diffusion coefficient and droplet radius) is equal to zero. The analysis presented in the paper is based on the method of integral manifolds and it allowed us to present the droplet evaporation rate as the sum of the evaporation rate predicted by the model based on the assumption that $\varepsilon = 0$ and the correction proportional to ε.

Applications

The correction proportional to ε is shown to be particularly important in the case of small water and methanol droplets (diameters less than 5 μm) evaporating in air at low pressure (0.1 atm.). In this case, this correction could reach 35% of the original evaporation rate. In the case of evaporation of relatively large droplets (with radii more than 10 μm) in air at atmospheric and higher pressures this corrections is shown to be small (less than 10^{-3} of the evaporation rate predicted by the model based on the assumption that $\varepsilon = 0$). This supports the results presented in [3].

Acknowledgments

The authors are grateful for the financial support received from Russian Science Foundation (Grant 21-19-00876) which supported S.S. Sazhin (who contributed to the preparation of the text of the abstract), E.A. Shchepakina, and V.A. Sobolev (who contributed to the development of the model).

References

[1] Cossali, G. and Tonini, S., 2021, “Drop Heating and Evaporation: Analytical Solutions in Curvilinear Coordinate Systems” Springer.
[2] Sazhin, S.S., 2022, “Droplets and Sprays: Simple Models of Complex Processes” Springer.
[3] Tonini S. and Cossali, G., 2012, Int. J. Therm. Sci., 57, 45.
[4] Tonini S., Cossali, G., Shchepakina, V. Sobolev, and Sazhin, S.S., 2022, Physics of Fluids, 34, 073312.
[5] Shchepakina, E., Sobolev, V. and Mortell, M., 2014, “Singular Perturbations: Introduction to System Order Reduction Methods with Applications” Springer.

Evaporation of multicomponent drops of general shape: analytical modeling through Stefan-Maxwell equations

S. Tonini*, G.E. Cossali
Department of Engineering and Applied Sciences, University of Bergamo, Italy
*Corresponding author: simona.tonini@unibg.it

Introduction

The poster presented at the 2022-DIPSI workshop reports about a model for drop heating and evaporation based on the analytical solution to the species conservation equations using the Stefan-Maxwell constitutive equations. The model can be applied to any drop shape, requiring only the existence of the solution of the Laplace equation with uniform Dirichlet boundary conditions on the boundaries of the gas domain. This model, reported in detail in [1], extends the one presented in [2], valid for ellipsoidal drops, to generally shaped liquid drops and drop structures.

Material and methods

The model reported in [1] and discussed here is based on an analytical solution to the Stefan-Maxwell (SM) equations for a generally shaped evaporating drop, generalising previous solutions for one dimensional cases to the case of multi-dimensional vapour fields. Constant properties and quasi-steadiness are assumed while convection, other than that due to Stefan flow, is neglected. In Stefan-Maxwell formulation

$$\mathbf{d}^{(p)} = \sum_{k=0}^{n} \frac{1}{cD_{pk}}\left(y^{(p)}\mathbf{N}^{(k)} - y^{(k)}\mathbf{N}^{(p)}\right) \tag{1}$$

(where $p=0$ stands for the non-evaporating gas species and $p>0$ for each of the evaporating species) the fluxes $N^{(p)}$ are implicitly dependent on the diffusional forces $d^{(p)}$, differently from the generalised Fick's law or the effective diffusivity formulations. The advantage of the SM formulation for this particular problem relies on the fact that the binary diffusion coefficients, D_{pk}, for dilute gases mixture are practically independent of mixture composition [3] and this allows the analytical solution of the species conservation equations in a relatively simple way.

The method is based on the solution of the following problem

$$\begin{aligned} &\nabla^2\Phi = 0 \\ &\Phi_s = 1; \quad \Phi_\infty = 0 \end{aligned} \tag{2}$$

Once Φ is known, the ansatz $N_j^{(p)} = C^{(p)}\nabla_j\Phi$ is used to obtain the solution of the species conservation equations, where the constants $C^{(p)}$ are found from the set of n trascendental equations

$$\left(A\Psi_s + \mathbf{B}\right) = e^A\left(A\Psi_\infty + \mathbf{B}\right) \tag{3}$$

Where

$$A = \begin{bmatrix} \sum_{q=1}^{n}\gamma_{1q}\hat{m}_{ev}^{(q)} & \hat{m}_{ev}^{(1)}\left(\gamma_{10}-\gamma_{12}\right) & \dots & \hat{m}_{ev}^{(1)}\left(\gamma_{10}-\gamma_{1n}\right) \\ \hat{m}_{ev}^{(2)}\left(\gamma_{20}-\gamma_{21}\right) & \sum_{q=1}^{n}\gamma_{2q}\hat{m}_{ev}^{(q)} & \dots & \hat{m}_{ev}^{(2)}\left(\gamma_{20}-\gamma_{2n}\right) \\ \dots & \dots & \dots & \dots \\ \hat{m}_{ev}^{(n)}\left(\gamma_{n0}-\gamma_{n1}\right) & \hat{m}_{ev}^{(n)}\left(\gamma_{n0}-\gamma_{n2}\right) & \dots & \sum_{q=1}^{n}\gamma_{nq}\hat{m}_{ev}^{(q)} \end{bmatrix}$$

$$\Psi = \left[y^{(1)} \quad \dots \quad y^{(n)}\right]^T \tag{4}$$

$$\mathbf{B} = -\left[\hat{m}_{ev}^{(1)}\gamma_{10} \quad \hat{m}_{ev}^{(2)}\gamma_{20} \quad \dots \quad \hat{m}_{ev}^{(n)}\gamma_{n0}\right]^T$$

that can be solved by numerical methods of relatively simple implementation. In (3) and (4), $y^{(p)}$ is the molar fraction of component p in the gas mixture, $\gamma_{pq} = \frac{D_{ref}}{D_{pq}}$ where D_{ref} is a reference dummy value for the diffusion coefficients, which has no influence on the final results, and the quantities $\hat{m}_{ev}^{(p)} = \frac{C^{(p)}}{cD_{ref}}$, proportional to the constants $C^{(p)}$, can be interpreted as non-dimensional form of the evaporation rates of each species. The latter can be promptly obtained from the relation (see [1] for further details and nomenclature for the meaning of other symbols)

$$m_{ev}^{(p)} = Mm^{(p)} cD_{ref} \hat{m}_{ev}^{(p)} \int_S \nabla_n \Phi dS \qquad (5)$$

It is noteworthy that the method allows solving also the steady state energy equation to yield the gas mixture temperature field in explicit form and the sensible heat rate exchanged between the drop and the ambient gas mixture as

$$T = \frac{T_s - T_\infty}{e^{\alpha} - 1}\left(e^{\alpha\Phi} - e^{\alpha}\right) + T_s \qquad (6a)$$

$$Q_s = -k_{ref}\,\alpha \frac{T_s - T_\infty}{e^{\alpha} - 1} e^{\alpha} \int_S \nabla_n \Phi dS \qquad (6b)$$

where $\alpha = \frac{\sum_{p=1}^{n} Mm^{(p)} C^{(p)} c_{p,ref}}{k_{ref}}$.

Results and Discussion

The above described analytical approach can be used to model the heating and evaporation of multi-component drops of virtually any shape. In particular, for all those cases where an analytical solution of equation (2) is available, the above reported way to calculate the evaporation rates is fully analytical.

The analytic form of Φ can be found in all those orthogonal curvilinear systems where the Laplace equation is separable, like spherical, prolate and oblate spheroidal, ellipsoidal, bispherical and toroidal coordinate systems (see [4] for details). Each of these special coordinate systems are used when modelling particular drop shapes (like spheroidal drops in spheroidal coordinates or sessile drops in toroidal coordinates) or drop dispositions (like pair of drops, even of different size, in bispherical coordinates). This yields many particular results related to the spatial distribution of the temperature and vapour concentrations fields, as for example the fact that all the species evaporation rates are proportional to the fourth root of the local Gaussian curvature for prolate and oblate spheroidal and triaxial ellipsoidal drop shapes (see [2]). However, some important results are independent of the drop shape. The ansatz $N_j^{(p)} = C^{(p)} \nabla_j \Phi$, which holds for any drop shape, was checked by implementing the numerical solution to ~~of~~ the conservation equations in COMSOL© and tested for various geometries, like those reported in figure 1 (to notice the case with four drops which does not admit any known analytical solution of equation (2)). One consequence of the ansatz is that there exists a unique dependence of the molar fractions of each component on the value of the function Φ. Figure 2 shows the results for the geometries of Figure 1, confirming this finding. Another general result, which can be derived from the above sketched theoretical approach, is that the ratios between the evaporation rates of each component are independent of the drop shape, although the absolute values depend on it. The mentioned ratios can actually be numerically found by only solving the transcendent equation (1), with no need to cope with the differential problem.

Furthermore, it can be observed that the relationships yielding the evaporation rates and the sensible heat rate (see equation 6) can be split into a part that depends on the boundary conditions (drop and gas temperature and drop composition) and the thermophysical properties of the gas mixture, and in another part (the integral $\int_S \nabla_n \Phi dS$), which is the same for both rates and it depends only on the drop shape.

The effect of choosing the SM equation as constitutive equation instead of the simpler, but approximate, effective diffusivity formulation, has been tested by comparing the maximum percentage relative difference between the evaporation rate predicted by the Stefan-Maxwell based model and that predicted by the effective diffusivity based model, $\Delta\% m_{ev}$. The values are plotted in Figure 3 as function of the parameter $\delta^{(1)} = D_{10} / \left(D_{10} + D_{20}\right)$, that is the ratio between the diffusion coefficient of the lighter component into the ambient gas and the sum of both the diffusion coefficients of each species present in the liquid phase, for 105 bi-component mixtures of alkanes (from C_6H_{14} to $C_{20}H_{42}$). The maximum discrepancies between the two approaches are of the order of 26%, and occur when the diffusivities of the two species in air have values close to each other. This analysis also shows that when the liquid mixture is almost single-component (i.e. one of the components strongly prevails on the other in the liquid mixture) and when the gas mixture is dilute (i.e. vapour concentrations in air at the drop surface is much smaller than 1), the two approaches yield close predictions, while in the other cases the predictions may be consistently different.

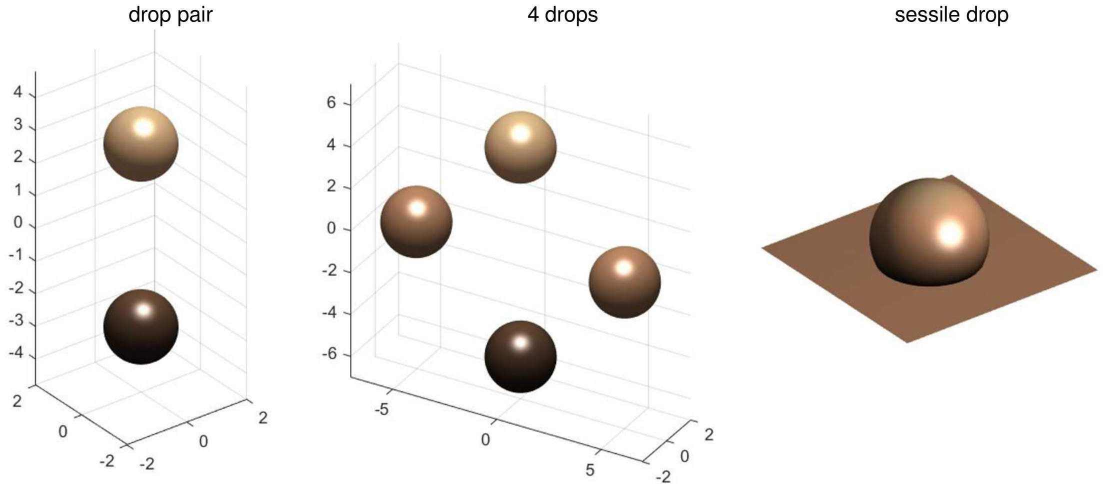

Figure 1. Drop shapes and structures used to test the model outcomes by numerical solving the species conservation equations using COMSOL ©.

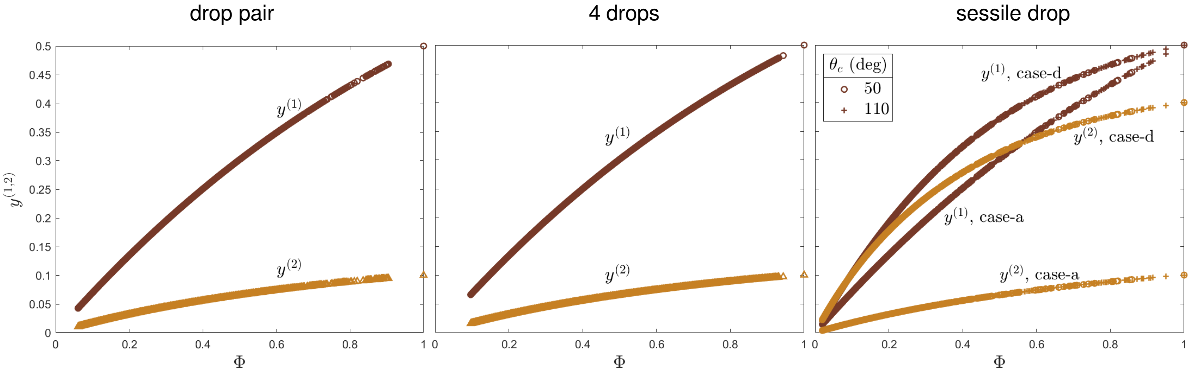

Figure 2. Molar fractions $y^{(p)}$ versus the values of the auxiliary function Φ over all the domain for two-components drops with the drop shape and configurations reported in figure 1.

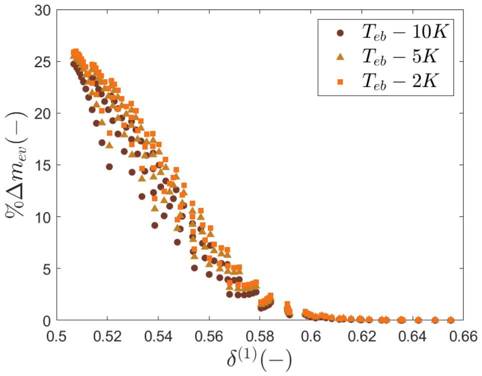

Figure 3. Percentage difference of the evaporation rate predicted by the present model and that predicted by the effective diffusivity approach as a function of $\delta^{(1)} = D_{10}/(D_{10} + D_{20})$ for 105 two-component liquid mixtures of 15 n-alkanes (from C_6H_{14} to $C_{20}H_{42}$) for gas temperature of 1000K and three different drop temperatures (T_{eb} is the boiling temperature of the lighter component).

Nomenclature

c	molar density [kmol m^{-3}]
$c_{p,ref}$	specific heat of gas mixture at reference temperature [J kg^{-1} K^{-1}]
D_{ref}, D_{pk}	diffusion coefficients [m^2 s^{-1}]
M_m	molar mass [kg kmol^{-1}]
k_{ref}	gas mixture conductivity at reference temperature [W m^{-1} K^{-1}]
Q	sensible heat rate [W]
T	temperature [K]

References

[1] 209) S. Tonini, G.E. Cossali, Modeling the evaporation of multicomponent drops of general shape on the basis of an analytical solution to the Stefan–Maxwell equations, Phys. Fluids 34, 073313 (2022)

[2] 204) S.Tonini, G.E. Cossali, An analytical model for the evaporation of multi-component spheroidal drops based on Stefan–Maxwell equations, International Journal of Thermal Sciences 171 (2022) 107223

[3] J.C. Slattery, "Momentum, energy and mass transfer in continua" (R. Krieger Publ., 1981).

[4] G.E. Cossali, S. Tonini; “Drop Heating and Evaporation: Analytical solutions in curvilinear coordinates”, Springer Nature Switzerland, 2021, Series Mathematical Engineering.

Mechanisms of sulphur capture by water spray systems

A. Amoresano*[1], G. Langella[2], S. Roscioli[2]
Department of Industrial Engineering, University of Naples Federico II, Italy
*Corresponding author: amedeo.amoresano@unina.it

Introduction

SO_X production by naval engines is a sensible environmental problem, hence it has been addressed by international regulations (Annex VI of MARPOL [1]). The regulation provides for the reduction of sulphur in the fuel up to a content equal to 5% by mass, meanwhile the actual SO_X emissions have to be controlled by external device like wet scrubbers.

This paper describes a numerical model to simulate SO_2 absorption phenomenon into a water droplet in a "wet scrubbing" process in dynamic conditions.

Material and methods

Two different numerical model to describe absorption phenomena of sulphur dioxide from water droplet into scrubbing tower were implemented. In both the case study is a single water droplet, totally hit by exhaust gas of typical marine engine, once in repose condition (fix approach, with stationary drop, constant droplet temperature, constant droplet volume) and the other one in variable condition (variable approach, with free fall down droplet, increasing droplet temperature, decreasing droplet volume).

Due to problematic chemical reactions between seawater and SO_2 for the alkalines content, freshwater droplet was examined and a simplified chemical model was used. The most important reaction which was considered is: [2]

$$SO_{2(aq)} + H_2O_{(l)} \rightleftharpoons HSO^-_{3(aq)} + H^+_{(aq)} \qquad (1)$$

which highlights the reaction between freshwater and sulphur dioxide, producing the bisulphite ion.

In both cases one – dimensional approach was supposed so only radial variation of SO_2 concentration can be considered not considering, obviously, the Hill vortex.

The analysis has been implemented for spray working with droplets in the range from 0.5×10^{-3} m to 2.0×10^{-3} m (with step of 0.5×10^{-3} m), with 500 K, 650 K and 750 K exhaust gases temperatures and with SO_2 concentration varying from 620 ppm to 920 ppm (with step of 100 ppm and supposing itself constant during the 3.2 seconds of each data processing)

The trend of ratio between mean concentration SO_2 and its concentration of saturation on the droplet surface has been evaluated. The analysis has been carried out for a monodisperse two phase fluid.

Results and Discussion

Taking into account the physical and chemical mechanisms, respectively mass diffusion (Henry law) and kinetic equations, their influence on absorption phenomenon has been analysed. The behaviour due to the interaction between water droplets and SO_X shows an absorption slow down. This is due to the limitation of the SO_2 incoming on the droplet surface. Furthermore the mass evaporation of the droplets increases the mean SO_2 concentration slowing down the inlet of the SO2 on the droplet surface (Figure 1).

Both, the internal diffusivity and the chemical reaction (1), permit to the new SO_2 molecules to go inside the water droplet. The production of the bisulphite ion involves the decreasing of the sulphur dioxide, because the diffusivity mechanism can be considered slower than the chemical reaction.

The SO_2 concentration is higher for the droplet with smaller diameter, so these reach a possible saturation condition faster than the others. The droplets about 0.5×10^{-3} m of diameter can be considered inadequate for the culling of the SO2 due to the rapid evaporation and the consequent transport with flue gases.

By numerical results it was deduced that a single drop with a smaller diameter tends to accumulate less quantity of sulphur dioxide, but this isn't an interesting outcome for practical use since into the scrubbing tower there isn't only a droplet. Therefore for each evaluation, a mass of water into the wet scrubber equal to a mass of a single water droplet with diameter 2.0×10^{-3} m was supposed in order to compare the absorption for each spray with different diameter. So for diameters 1.0×10^{-3} m and 1.5×10^{-3} m the N_i number of droplet to reaches the mass of water droplet with 2.0×10^{-3} m diameter was calculated, resulting that for the firsts were necessary 8 droplets and for the seconds 2.37 droplets.

The computation shows that the droplets with the smaller diameter were able to absorb more sulphur dioxide than the others with the same mass because surface-volume ratio is higher, arriving at 3.42×10^{-4} g approximately for the 8 droplets with diameter 1.0 x 10^{-3} m at time 3.2 s in the variable approach, compared to 4.81 x 10^{-5} g of the droplet with diameter 2.0 x 10^{-3} m at the same conditions regarding flue gas characteristics, in other word SO_2 concentration equal to 620 ppm and temperature equal to 750 K (Figure 2).

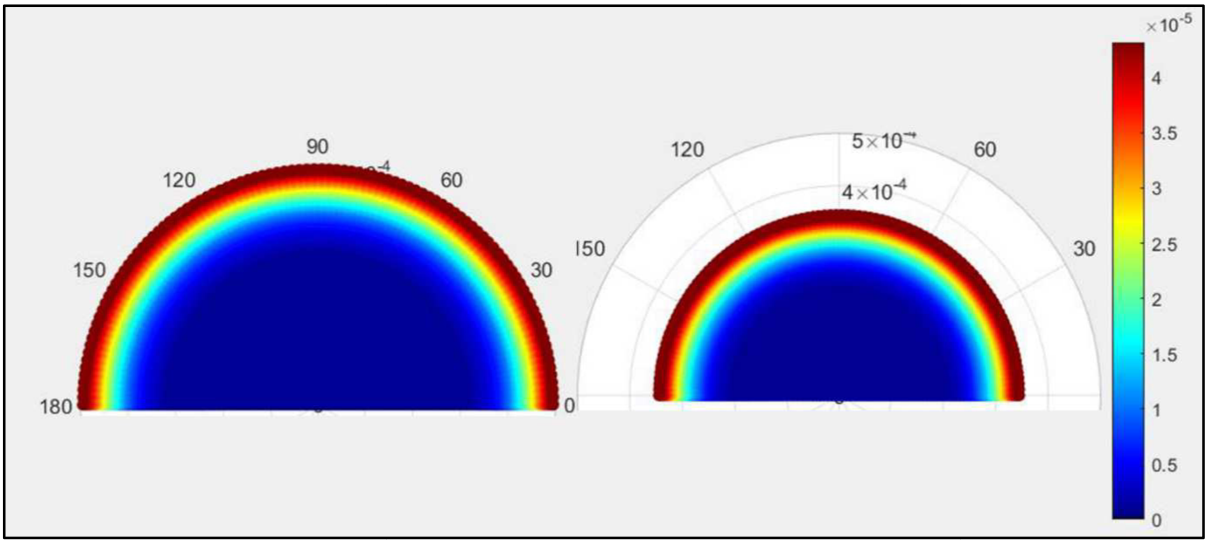

Figure 1. Comparison between fix (left) and variable (right) approaches for the evaluation of SO_2 concentration [kmol/m^3] at t=3.2 s of simulation, C_g=620 ppm, $d_{p,st}$= 1.0 x 10^{-3} m, T_g=750 K

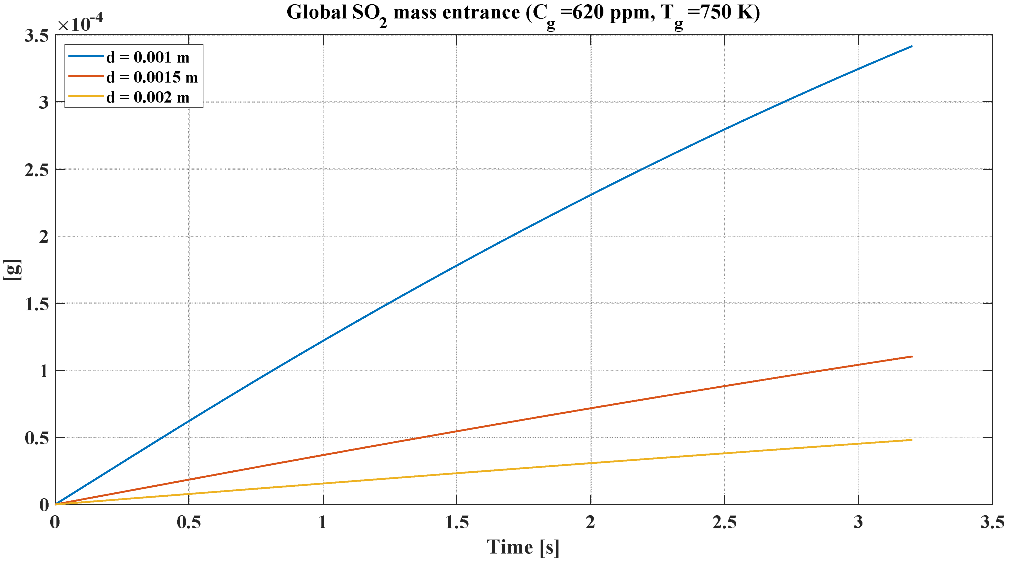

Figure 2. Global SO_2 mass entrance for the N_i droplets at C_g = 620 ppm, T_g = 750 K, $N_{1.0}$ = 8, $N_{1.5}$ = 2.37

Trends in Figure 2 are a bit curved due to the faster evaporation of the droplets, which implicates less SO_2 mass absorbed than computation with lower temperature. At the same external concentration of sulphur dioxide and time, at the temperature of 500 K (typical values for naval engines) indeed absorbed mass was 3.8 x 10^{-4} g for the water droplets with diameter 1.0 x 10^{-3} m and 4.9 x 10^{-5} g for the drop with diameter 2.0 x 10-3 m.

Exhaust gases SO_2 concentration has however a more incisive weight than temperature of themselves, in fact at C_g = 920 ppm (non-recurring value) and T_g = 500 K $\mathbf{SO_2}$ mass absorbed from droplets with diameter 1.0 x 10^{-3} m was 5.52 x 10^{-4} g, while from droplet with diameter 2.0 x 10^{-3} m was 7.17 x 10^{-5} g.

Nomenclature

C_g	SO_2 concentration in exhaust gases [ppm]
$d_{p,st}$	starting droplet diameter [m]
t	time [s]
T_g	exhaust gases temperature [K]
N_i	number of droplets with diameter equal to i x 10^{-3} m to reaches the mass of water droplet with 2.0 x 10^{-3} m diameter

References

[1] IMO - International Maritime Organizzation, “MARPOL - Annex VI,” [Online]. Available: http://www.imo.org.

[2] A. Saboni and S. Alexandrova, “Sulfur dioxide absorption and desorption by water drops,” Chemical Engineering Journal, 2001.

Author index

Progetto grafico:
Servizi Editoriali – Università degli Studi di Bergamo
Università degli Studi di Bergamo
via Salvecchio, 19
24129 Bergamo
Cod. Fiscale 80004350163
P. IVA 0161280016